

01 Jun 2011

Search for Gravitational Waves from Binary Black Hole Inspiral, Merger, and Ringdown

J. Abadie

Marco Cavaglia

Missouri University of Science and Technology, cavagliam@mst.edu

For full list of authors, see publisher's website.

Follow this and additional works at: https://scholarsmine.mst.edu/phys_facwork

 Part of the [Physics Commons](#)

Recommended Citation

J. Abadie et al., "Search for Gravitational Waves from Binary Black Hole Inspiral, Merger, and Ringdown," *Physical Review D - Particles, Fields, Gravitation and Cosmology*, vol. 83, no. 12, American Physical Society (APS), Jun 2011.

The definitive version is available at <https://doi.org/10.1103/PhysRevD.83.122005>

This Article - Journal is brought to you for free and open access by Scholars' Mine. It has been accepted for inclusion in Physics Faculty Research & Creative Works by an authorized administrator of Scholars' Mine. This work is protected by U. S. Copyright Law. Unauthorized use including reproduction for redistribution requires the permission of the copyright holder. For more information, please contact scholarsmine@mst.edu.

Search for gravitational waves from binary black hole inspiral, merger, and ringdown

J. Abadie,^{29,a} B. P. Abbott,^{29,a} R. Abbott,^{29,a} M. Abernathy,^{67,a} T. Accadia,^{27,b} F. Acernese,^{19a,19c,b} C. Adams,^{31,a} R. Adhikari,^{29,a} P. Ajith,^{29,a} B. Allen,^{2,79,a} G. S. Allen,^{53,a} E. Amador Ceron,^{79,a} R. S. Amin,^{34,a} S. B. Anderson,^{29,a} W. G. Anderson,^{79,a} F. Antonucci,^{22a,b} M. A. Arain,^{66,a} M. C. Araya,^{29,a} M. Aronsson,^{29,a} Y. Aso,^{29,a} S. M. Aston,^{65,a} P. Astone,^{22a,b} D. Atkinson,^{30,a} P. Aufmuth,^{28,2,a} C. Aulbert,^{2,28,a} S. Babak,^{1,a} P. Baker,^{37,a} G. Ballardin,^{13,b} T. Ballinger,^{10,a} S. Ballmer,^{29,a} D. Barker,^{30,a} S. Barnum,^{32,a} F. Barone,^{19a,19c,b} B. Barr,^{67,a} P. Barriga,^{78,a} L. Barsotti,^{32,a} M. Barsuglia,^{4,b} M. A. Barton,^{30,a} I. Bartos,^{12,a} R. Bassiri,^{67,a} M. Bastarrika,^{67,a} J. Bauchrowitz,^{2,28,a} Th. S. Bauer,^{41a,b} B. Behnke,^{1,a} M. G. Beker,^{41a,b} A. Belletoile,^{27,b} M. Benacquista,^{60,a} A. Bertolini,^{2,28,a} J. Betzwieser,^{29,a} N. Beveridge,^{67,a} P. T. Beyersdorf,^{49,a} I. A. Bilenko,^{38,a} G. Billingsley,^{29,a} J. Birch,^{31,a} S. Birindelli,^{43a,b} R. Biswas,^{79,a} M. Bitossi,^{21a,b} M. A. Bizouard,^{26a,b} E. Black,^{29,a} J. K. Blackburn,^{29,a} L. Blackburn,^{32,a} D. Blair,^{78,a} B. Bland,^{30,a} M. Blom,^{41a,b} C. Boccara,^{26b,b} O. Bock,^{2,28,a} T. P. Bodiya,^{32,a} R. Bondarescu,^{55,a} F. Bondu,^{43b,b} L. Bonelli,^{21a,21b,b} R. Bonnand,^{33,b} R. Bork,^{29,a} M. Born,^{2,28,a} V. Boschi,^{21a,b} S. Bose,^{80,a} L. Bosi,^{20a,b} B. Bouhou,^{4,b} M. Boyle,^{8,a} S. Braccini,^{21a,b} C. Bradaschia,^{21a,b} P. R. Brady,^{79,a} V. B. Braginsky,^{38,a} J. E. Brau,^{72,a} J. Breyer,^{2,28,a} D. O. Bridges,^{31,a} A. Brillet,^{43a,b} M. Brinkmann,^{2,28,a} V. Brisson,^{26a,b} M. Britzger,^{2,28,a} A. F. Brooks,^{29,a} D. A. Brown,^{54,a} R. Budzyński,^{45b,b} T. Bulik,^{45c,45d,b} H. J. Bulten,^{41a,41b,b} A. Buonanno,^{68,a} J. Burguet-Castell,^{79,a} O. Burmeister,^{2,28,a} D. Buskulic,^{27,b} C. Buy,^{4,b} R. L. Byer,^{53,a} L. Cadonati,^{69,a} G. Cagnoli,^{17a,b} J. Cain,^{57,a} E. Calloni,^{19a,19b,b} J. B. Camp,^{39,a} E. Campagna,^{17a,17b,b} P. Campsie,^{67,a} J. Cannizzo,^{39,a} K. Cannon,^{29,a} B. Canuel,^{13,b} J. Cao,^{62,a} C. Capano,^{54,a} F. Carbognani,^{13,b} S. Caride,^{70,a} S. Caudill,^{34,a} M. Cavaglià,^{57,a} F. Cavalier,^{26a,b} R. Cavalieri,^{13,b} G. Cella,^{21a,b} C. Cepeda,^{29,a} E. Cesarini,^{17b,b} O. Chaibi,^{43a,b} T. Chalermongsak,^{29,a} E. Chalkley,^{67,a} P. Charlton,^{11,a} E. Chassande-Mottin,^{4,b} S. Chelkowski,^{65,a} Y. Chen,^{8,a} A. Chincarini,^{18,b} N. Christensen,^{10,a} S. S. Y. Chua,^{5,a} C. T. Y. Chung,^{56,a} D. Clark,^{53,a} J. Clark,^{9,a} J. H. Clayton,^{79,a} F. Cleva,^{43a,b} E. Coccia,^{23a,23b,b} C. N. Colacino,^{21a,21b,b} J. Colas,^{13,b} A. Colla,^{22a,22b,b} M. Colombini,^{22b,b} R. Conte,^{74,a} D. Cook,^{30,a} T. R. Corbitt,^{32,a} N. Cornish,^{37,a} A. Corsi,^{22a,b} C. A. Costa,^{34,a} J.-P. Coulon,^{43a,b} D. M. Coward,^{78,a} D. C. Coyne,^{29,a} J. D. E. Creighton,^{79,a} T. D. Creighton,^{60,a} A. M. Cruise,^{65,a} R. M. Culter,^{65,a} A. Cumming,^{67,a} L. Cunningham,^{67,a} E. Cuoco,^{13,b} K. Dahl,^{2,28,a} S. L. Danilishin,^{38,a} R. Dannenberg,^{29,a} S. D'Antonio,^{23a,b} K. Danzmann,^{2,28,a} K. Das,^{66,a} V. Dattilo,^{13,b} B. Daudert,^{29,a} M. Davier,^{26a,b} G. Davies,^{9,a} A. Davis,^{14,a} E. J. Daw,^{58,a} R. Day,^{13,b} T. Dayanga,^{80,a} R. DeRosa,^{19a,19b,b} D. DeBra,^{53,a} G. Debreczeni,^{46,b} J. Degallaix,^{2,28,a} M. del Prete,^{21a,21c,b} V. Dergachev,^{29,a} R. De Rosa,^{34,a} R. DeSalvo,^{29,a} P. Devanka,^{9,a} S. Dhurandhar,^{25,a} L. Di Fiore,^{19a,b} A. Di Lieto,^{21a,21b,b} I. Di Palma,^{2,28,a} M. Di Paolo Emilio,^{23a,23c,b} A. Di Virgilio,^{21a,b} M. Díaz,^{60,a} A. Dietz,^{27,b} F. Donovan,^{32,a} K. L. Dooley,^{66,a} E. E. Doomes,^{52,a} S. Dorsher,^{71,a} E. S. D. Douglas,^{30,a} M. Drago,^{44c,44d,b} R. W. P. Drever,^{6,a} J. C. Driggers,^{29,a} J. Dueck,^{2,a} J.-C. Dumas,^{78,a} S. Dwyer,³² T. Eberle,^{2,28,a} M. Edgar,^{67,a} M. Edwards,^{9,a} A. Effler,^{34,a} P. Ehrens,^{29,a} G. Ely,^{10,a} R. Engel,^{29,a} T. Etzel,^{29,a} M. Evans,^{32,a} T. Evans,^{31,a} V. Fafone,^{23a,23b,b} S. Fairhurst,^{9,a} Y. Fan,^{78,a} B. F. Farr,^{42,a} D. Fazi,^{42,a} H. Fehrmann,^{2,28,a} D. Feldbaum,^{66,a} I. Ferrante,^{21a,21b,b} F. Fidecaro,^{21a,21b,b} L. S. Finn,^{55,a} I. Fiori,^{13,b} R. Flaminio,^{33,b} M. Flanigan,^{30,a} K. Flasch,^{79,a} S. Foley,^{32,a} C. Forrest,^{73,a} E. Forsi,^{31,a} L. A. Forte,^{19a,b} N. Fotopoulos,^{79,a} J.-D. Fournier,^{43a,b} J. Franc,^{33,b} S. Frasca,^{22a,22b,b} F. Frasconi,^{21a,b} M. Frede,^{2,28,a} M. Frei,^{59,a} Z. Frei,^{15,a} A. Freise,^{65,a} R. Frey,^{72,a} T. T. Fricke,^{34,a} D. Friedrich,^{2,28,a} P. Fritschel,^{32,a} V. V. Frolov,^{31,a} P. Fulda,^{65,a} M. Fyffe,^{31,a} M. Galimberti,^{33,b} L. Gammaitoni,^{20a,20b,b} J. A. Garofoli,^{54,a} F. Garufi,^{19a,19b,b} M. E. Gáspár,^{46,b} G. Gemme,^{18,b} E. Genin,^{13,b} A. Gennai,^{21a,b} I. Gholami,^{1,a} S. Ghosh,^{80,a} J. A. Giaime,^{34,31,a} S. Giampanis,^{2,28,a} K. D. Giardino,^{31,a} A. Giazotto,^{21a,b} C. Gill,^{67,a} E. Goetz,^{70,a} L. M. Goggin,^{79,a} G. González,^{34,a} M. L. Gorodetsky,^{38,a} S. Goßler,^{2,28,a} R. Gouaty,^{27,b} C. Graef,^{2,28,a} M. Granata,^{4,b} A. Grant,^{67,a} S. Gras,^{78,a} C. Gray,^{30,a} R. J. S. Greenhalgh,^{48,a} A. M. Gretarsson,^{14,a} C. Greverie,^{43a,b} R. Grosso,^{60,a} H. Grote,^{2,28,a} S. Grunewald,^{1,a} G. M. Guidi,^{17a,17b,b} E. K. Gustafson,^{29,a} R. Gustafson,^{70,a} B. Hage,^{28,2,a} P. Hall,^{9,a} J. M. Hallam,^{65,a} D. Hammer,^{79,a} G. Hammond,^{67,a} J. Hanks,^{30,a} C. Hanna,^{29,a} J. Hanson,^{31,a} J. Harms,^{6,a} G. M. Harry,^{32,a} I. W. Harry,^{9,a} E. D. Harstad,^{72,a} K. Haughian,^{67,a} K. Hayama,^{40,a} J.-F. Hayau,^{43b,b} T. Hayler,^{48,a} J. Heefner,^{29,a} H. Heitmann,^{43a,b} P. Hello,^{26a,b} I. S. Heng,^{67,a} A. W. Heptonstall,^{29,a} M. Hewitson,^{2,28,a} S. Hild,^{67,a} E. Hirose,^{54,a} D. Hoak,^{69,a} K. A. Hodge,^{29,a} K. Holt,^{31,a} D. J. Hosken,^{64,a} J. Hough,^{67,a} E. J. Howell,^{78,a} D. Hoyland,^{65,a} D. Huet,^{13,b} B. Hughey,^{32,a} S. Husa,^{63,a} S. H. Huttner,^{67,a} T. Huynh-Dinh,^{31,a} D. R. Ingram,^{30,a} R. Inta,^{5,a} T. Isogai,^{10,a} A. Ivanov,^{29,a} P. Jaranowski,^{45e,b} W. W. Johnson,^{34,a} D. I. Jones,^{76,a} G. Jones,^{9,a} R. Jones,^{67,a} L. Ju,^{78,a} P. Kalmus,^{29,a} V. Kalogera,^{42,a} S. Kandhasamy,^{71,a} J. B. Kanner,^{68,a} E. Katsavounidis,^{32,a} K. Kawabe,^{30,a} S. Kawamura,^{40,a} F. Kawazoe,^{2,28,a} W. Kells,^{29,a} D. G. Keppel,^{29,a} A. Khalaidovski,^{2,28,a} F. Y. Khalili,^{38,a} E. A. Khazanov,^{24,a} H. Kim,^{2,28,a} P. J. King,^{29,a} D. L. Kinzel,^{31,a} J. S. Kissel,^{34,a} S. Klimenko,^{66,a} V. Kondrashov,^{29,a} R. Kopparapu,^{55,a} S. Koranda,^{79,a} I. Kowalska,^{45c,b} D. Kozak,^{29,a} T. Krause,^{59,a} V. Kringel,^{2,28,a}

- S. Krishnamurthy,^{42,a} B. Krishnan,^{1,a} A. Królak,^{45a,45f,b} G. Kuehn,^{2,28,a} J. Kullman,^{2,a} R. Kumar,^{67,a}
P. Kwee,^{28,2,a} M. Landry,^{30,a} M. Lang,^{55,a} B. Lantz,^{53,a} N. Lastzka,^{2,28,a} A. Lazzarini,^{29,a} P. Leaci,^{1,a} J. Leong,^{2,28,a}
I. Leonor,^{72,a} N. Leroy,^{26a,b} N. Letendre,^{27,b} J. Li,^{60,a} T. G. F. Li,^{41a,b} N. Liguori,^{44a,44b,b} H. Lin,^{66,a} P. E. Lindquist,^{29,a}
N. A. Lockerbie,^{77,a} D. Lodhia,^{65,a} M. Lorenzini,^{17a,b} V. Loriette,^{26b,b} M. Lormand,^{31,a} G. Losurdo,^{17a,b}
P. Lu,^{53,a} J. Luan,^{8,a} M. Lubinski,^{30,a} A. Lucianetti,^{66,a} H. Lück,^{22a,b} A. D. Lundgren,^{54,a} B. Machenschalk,^{2,28,a}
M. MacInnis,^{32,a} M. Mageswaran,^{29,a} K. Mailand,^{29,a} E. Majorana,^{22a,b} C. Mak,^{29,a} I. Maksimovic,^{26b,b} N. Man,^{43a,b}
I. Mandel,^{42,a} V. Mandic,^{71,a} M. Mantovani,^{21a,21c,b} F. Marchesoni,^{20a,b} F. Marion,^{27,b} S. Márka,^{12,a} Z. Márka,^{12,a}
E. Maros,^{29,a} J. Marque,^{13,b} F. Martelli,^{17a,17b,b} I. W. Martin,^{67,a} R. M. Martin,^{66,a} J. N. Marx,^{29,a} K. Mason,^{32,a}
A. Masserot,^{27,b} F. Matichard,^{32,a} L. Matone,^{12,a} R. A. Matzner,^{59,a} N. Mavalvala,^{32,a} R. McCarthy,^{30,a} D. E. McClelland,^{5,a}
S. C. McGuire,^{52,a} G. McIntyre,^{29,a} G. McIvor,^{59,a} D. J. A. McKechnan,^{9,a} G. Meadors,^{70,a} M. Mehmet,^{2,28,a} T. Meier,^{28,2,a}
A. Melatos,^{56,a} A. C. Melissinos,^{73,a} G. Mendell,^{30,a} D. F. Menéndez,^{55,a} R. A. Mercer,^{79,a} L. Merill,^{78,a} S. Meshkov,^{29,a}
C. Messenger,^{2,28,a} M. S. Meyer,^{31,a} H. Miao,^{78,a} C. Michel,^{33,b} L. Milano,^{19a,19b,b} J. Miller,^{67,a} Y. Minenkov,^{23a,b}
Y. Mino,^{8,a} S. Mitra,^{29,a} V. P. Mitrofanov,^{38,a} G. Mitselmakher,^{66,a} R. Mittleman,^{32,a} B. Moe,^{79,a} M. Mohan,^{13,b}
S. D. Mohanty,^{60,a} S. R. P. Mohapatra,^{69,a} D. Moraru,^{30,a} J. Moreau,^{26b,b} G. Moreno,^{30,a} N. Morgado,^{33,b}
A. Morgia,^{23a,23b,b} T. Morioka,^{40,a} K. Mors,^{2,a} S. Mosca,^{19a,19b,b} V. Moscatelli,^{22a,b} K. Mossavi,^{2,28,a} B. Mours,^{27,b}
C. M. Mow-Lowry,^{5,a} G. Mueller,^{66,a} S. Mukherjee,^{60,a} A. Mullavey,^{5,a} H. Müller-Ebhardt,^{2,28,a} J. Munch,^{64,a}
P. G. Murray,^{67,a} T. Nash,^{29,a} R. Nawrodt,^{67,a} J. Nelson,^{67,a} I. Neri,^{20a,20b,b} G. Newton,^{67,a} A. Nishizawa,^{40,a} F. Nocera,^{13,b}
D. Nolting,^{31,a} E. Ochsner,^{68,a} J. O'Dell,^{48,a} G. H. Ogin,^{29,a} R. G. Oldenburg,^{79,a} B. O'Reilly,^{31,a}
R. O'Shaughnessy,^{55,a} C. Osthelder,^{29,a} D. J. Ottaway,^{64,a} R. S. Ottens,^{66,a} H. Overmier,^{31,a} B. J. Owen,^{55,a} A. Page,^{65,a}
G. Pagliaroli,^{23a,23c,b} L. Palladino,^{23a,23c,b} C. Palomba,^{22a,b} Y. Pan,^{68,a} C. Pankow,^{66,a} F. Paoletti,^{21a,13,b} M. A. Papa,^{1,79,a}
S. Pardi,^{19a,19b,b} M. Pareja,^{2,28,a} M. Parisi,^{19a,19b,b} A. Pasqualetti,^{13,b} R. Passaquieti,^{21a,21b,b} D. Passuello,^{21a,b} P. Patel,^{29,a}
D. Pathak,^{9,a} M. Pedraza,^{29,a} L. Pekowsky,^{54,a} S. Penn,^{16,a} C. Peralta,^{1,a} A. Perreca,^{65,a} G. Persichetti,^{19a,19b,b}
M. Pichot,^{43a,b} M. Pickenpack,^{2,28,a} F. Piergiovanni,^{17a,17b,b} M. Pietka,^{45c,b} L. Pinard,^{33,b} I. M. Pinto,^{75,a} M. Pitkin,^{67,a}
H. J. Pletsch,^{2,28,a} M. V. Plissi,^{67,a} R. Poggiani,^{21a,21b,b} F. Postiglione,^{74,a} M. Prato,^{18,b} V. Predoi,^{9,a} L. R. Price,^{79,a}
M. Prijatelj,^{2,28,a} M. Principe,^{75,a} R. Prix,^{2,28,a} G. A. Prodi,^{44a,44b,b} L. Prokhorov,^{38,a} O. Puncken,^{2,28,a} M. Punturo,^{20a,b}
P. Puppo,^{22a,b} V. Quetschke,^{60,a} F. J. Raab,^{30,a} D. S. Rabeling,^{41a,41b,b} I. Rácz,^{46,b} T. Radke,^{1,a} H. Radkins,^{30,a} P. Raffai,^{15,a}
M. Rakhmanov,^{60,a} B. Rankins,^{57,a} P. Rapagnani,^{22a,22b,b} V. Raymond,^{42,a} V. Re,^{44a,44b,b} C. M. Reed,^{30,a} T. Reed,^{35,a}
T. Regimbau,^{43a,b} S. Reid,^{67,a} D. H. Reitze,^{66,a} F. Ricci,^{22a,22b,b} R. Riesen,^{31,a} K. Riles,^{70,a} P. Roberts,^{3,a}
N. A. Robertson,^{29,67} F. Robinet,^{26a,b} C. Robinson,^{9,a} E. L. Robinson,^{1,a} A. Rocchi,^{23a,b} S. Roddy,^{31,a} L. Rolland,^{27,b}
J. Rollins,^{12,a} J. D. Romano,^{60,a} R. Romano,^{19a,19c,b} J. H. Romie,^{31,a} D. Rosińska,^{45g,b} C. Röver,^{2,28,a} S. Rowan,^{67,a}
A. Rüdiger,^{2,28,a} P. Ruggi,^{13,b} K. Ryan,^{30,a} S. Sakata,^{40,a} M. Sakosky,^{30,a} F. Salemi,^{2,28,a} L. Sammut,^{56,a}
L. Sancho de la Jordana,^{63,a} V. Sandberg,^{30,a} V. Sannibale,^{29,a} L. Santamaría,^{1,a} G. Santostasi,^{36,a} S. Saraf,^{50,a}
B. Sassolas,^{33,b} B. S. Sathyaprakash,^{9,a} S. Sato,^{40,a} M. Satterthwaite,^{5,a} P. R. Saulson,^{54,a} R. Savage,^{30,a}
R. Schilling,^{2,28,a} R. Schnabel,^{2,28,a} R. M. S. Schofield,^{72,a} B. Schulz,^{2,28,a} B. F. Schutz,^{1,9,a} P. Schwinberg,^{30,a} J. Scott,^{67,a}
S. M. Scott,^{5,a} A. C. Searle,^{29,a} F. Seifert,^{29,a} D. Sellers,^{31,a} A. S. Sengupta,^{29,a} D. Sentenac,^{13,b} A. Sergeev,^{24,a}
D. A. Shaddock,^{5,a} B. Shapiro,^{32,a} P. Shawhan,^{68,a} D. H. Shoemaker,^{32,a} A. Sibley,^{31,a} X. Siemens,^{79,a} D. Sigg,^{30,a}
A. Singer,^{29,a} A. M. Sintes,^{63,a} G. Skelton,^{79,a} B. J. J. Slagmolen,^{5,a} J. Slutsky,^{34,a} J. R. Smith,^{7,a} M. R. Smith,^{29,a}
N. D. Smith,^{32,a} K. Somiya,^{8,a} B. Sorazu,^{67,a} F. C. Speirits,^{67,a} L. Sperandio,^{23a,23b,b} A. J. Stein,^{32,a} L. C. Stein,^{32,a}
S. Steinlechner,^{2,28,a} S. Steplewski,^{80,a} A. Stochino,^{29,a} R. Stone,^{60,a} K. A. Strain,^{67,a} S. Strigin,^{38,a} A. S. Stroer,^{39,a}
R. Sturani,^{17a,17b,b} A. L. Stuver,^{31,a} T. Z. Summerscales,^{3,a} M. Sung,^{34,a} S. Susmithan,^{78,a} P. J. Sutton,^{9,a} B. Swinkels,^{13,b}
G. P. Szokoly,^{15,a} M. Tacca,^{13,b} D. Talukder,^{80,a} D. B. Tanner,^{66,a} S. P. Tarabrin,^{2,28,a} J. R. Taylor,^{2,28,a} R. Taylor,^{29,a}
P. Thomas,^{30,a} K. A. Thorne,^{31,a} K. S. Thorne,^{8,a} E. Thrane,^{71,a} A. Thüring,^{28,2,a} C. Titsler,^{55,a} K. V. Tokmakov,^{67,77,a}
A. Toncelli,^{21a,21b,b} M. Tonelli,^{21a,21b,b} O. Torre,^{21a,21c,b} C. Torres,^{31,a} C. I. Torrie,^{29,67} E. Tournefier,^{27,b}
F. Travasso,^{20a,20b,b} G. Traylor,^{31,a} M. Trias,^{63,a} K. Tseng,^{53,a} L. Turner,^{29,a} D. Ugolini,^{61,a} K. Urbanek,^{53,a}
H. Vahlbruch,^{28,2,a} B. Vaishnav,^{60,a} G. Vajente,^{21a,21b,b} M. Vallisneri,^{8,a} J. F. J. van den Brand,^{41a,41b,b}
C. Van Den Broeck,^{41a,b} S. van der Putten,^{41a,b} M. V. van der Sluys,^{42,a} A. A. van Veggel,^{67,a} S. Vass,^{29,a} M. Vasuth,^{46,b}
R. Vaulin,^{79,a} M. Vavoulidis,^{26a,b} A. Vecchio,^{65,a} G. Vedovato,^{44c,b} J. Veitch,^{9,a} P. J. Veitch,^{64,a} C. Veltkamp,^{2,28,a}
D. Verkindt,^{27,b} F. Vetrano,^{17a,17b,b} A. Viceré,^{17a,17b,b} A. E. Villar,^{29,a} J.-Y. Vinet,^{43a,b} H. Vocca,^{20a,b} C. Vorvick,^{30,a}
S. P. Vyachanin,^{38,a} S. J. Waldman,^{32,a} L. Wallace,^{29,a} A. Wanner,^{2,28,a} R. L. Ward,^{29,a} M. Was,^{26a,b} P. Wei,^{54,a}
M. Weinert,^{2,28,a} A. J. Weinstein,^{29,a} R. Weiss,^{32,a} L. Wen,^{8,78,a} S. Wen,^{34,a} P. Wessels,^{2,28,a} M. West,^{54,a}
T. Westphal,^{2,28,a} K. Wette,^{5,a} J. T. Whelan,^{47,a} S. E. Whitcomb,^{29,a} D. White,^{58,a} B. F. Whiting,^{66,a} C. Wilkinson,^{30,a}

P. A. Willems,^{29,a} L. Williams,^{66,a} B. Willke,^{2,28,a} L. Winkelmann,^{2,28,a} W. Winkler,^{2,28,a}
 C. C. Wipf,^{32,a} A. G. Wiseman,^{79,a} G. Woan,^{67,a} R. Wooley,^{31,a} J. Worden,^{30,a} I. Yakushin,^{31,a}
 H. Yamamoto,^{29,a} K. Yamamoto,^{2,28,a} D. Yeaton-Massey,^{29,a} S. Yoshida,^{51,a} P. Yu,^{79,a} M. Yvert,^{27,b}
 M. Zanolin,^{14,a} L. Zhang,^{29,a} Z. Zhang,^{78,a} C. Zhao,^{78,a} N. Zotov,^{35,a}
 M. E. Zucker,^{32,a} and J. Zweizig^{2,a}

(^aLIGO Scientific Collaboration)

(^bVirgo Collaboration)

- ¹Albert-Einstein-Institut, Max-Planck-Institut für Gravitationsphysik, D-14476 Golm, Germany
²Albert-Einstein-Institut, Max-Planck-Institut für Gravitationsphysik, D-30167 Hannover, Germany
³Andrews University, Berrien Springs, Michigan 49104, USA
⁴Laboratoire AstroParticule et Cosmologie (APC), Université Paris Diderot, CNRS: IN2P3, CEA: DSM/IRFU, Observatoire de Paris, 10 rue A. Domon et L. Duquet, 75013 Paris, France
⁵Australian National University, Canberra, 0200, Australia
⁶California Institute of Technology, Pasadena, California 91125, USA
⁷California State University Fullerton, Fullerton, California 92831, USA
⁸Caltech-CaRT, Pasadena, California 91125, USA
⁹Cardiff University, Cardiff, CF24 3AA, United Kingdom
¹⁰Carleton College, Northfield, Minnesota 55057, USA
¹¹Charles Sturt University, Wagga Wagga, NSW 2678, Australia
¹²Columbia University, New York, New York 10027, USA
¹³European Gravitational Observatory (EGO), I-56021 Cascina (PI), Italy
¹⁴Embry-Riddle Aeronautical University, Prescott, Arizona 86301, USA
¹⁵Eötvös Loránd University, Budapest, 1117 Hungary
¹⁶Hobart and William Smith Colleges, Geneva, New York 14456, USA
^{17a}INFN, Sezione di Firenze, I-50019 Sesto Fiorentino, Italy
^{17b}Università degli Studi di Urbino 'Carlo Bo', I-61029 Urbino, Italy
¹⁸INFN, Sezione di Genova; I-16146 Genova, Italy
^{19a}INFN, Sezione di Napoli, Italy
^{19b}Università di Napoli 'Federico II', Complesso Universitario di Monte S. Angelo, I-80126 Napoli, Italy
^{19c}Università di Salerno, Fisciano, I-84084 Salerno, Italy
^{20a}INFN, Sezione di Perugia, I-06123 Perugia, Italy
^{20b}Università di Perugia, I-06123 Perugia, Italy
^{21a}INFN, Sezione di Pisa, Italy
^{21b}Università di Pisa, I-56127 Pisa, Italy
^{21c}Università di Siena, I-53100 Siena, Italy
^{22a}INFN, Sezione di Roma, Italy
^{22b}Università 'La Sapienza', I-00185 Roma, Italy
^{23a}INFN, Sezione di Roma Tor Vergata, Italy
^{23b}Università di Roma Tor Vergata, I-00133 Roma, Italy
^{23c}Università dell'Aquila, I-67100 L'Aquila, Italy
²⁴Institute of Applied Physics, Nizhny Novgorod, 603950, Russia
²⁵Inter-University Centre for Astronomy and Astrophysics, Pune - 411007, India
^{26a}LAL, Université Paris-Sud, IN2P3/CNRS, F-91898 Orsay, France
^{26b}ESPCI, CNRS, F-75005 Paris, France
²⁷Laboratoire d'Annecy-le-Vieux de Physique des Particules (LAPP), Université de Savoie, CNRS/IN2P3, F-74941 Annecy-Le-Vieux, France
²⁸Leibniz Universität Hannover, D-30167 Hannover, Germany
²⁹LIGO - California Institute of Technology, Pasadena, California 91125, USA
³⁰LIGO - Hanford Observatory, Richland, Washington 99352, USA
³¹LIGO - Livingston Observatory, Livingston, Louisiana 70754, USA
³²LIGO - Massachusetts Institute of Technology, Cambridge, Massachusetts 02139, USA
³³Laboratoire des Matériaux Avancés (LMA), IN2P3/CNRS, F-69622 Villeurbanne, Lyon, France
³⁴Louisiana State University, Baton Rouge, Louisiana 70803, USA
³⁵Louisiana Tech University, Ruston, Louisiana 71272, USA
³⁶McNeese State University, Lake Charles, Louisiana 70609, USA
³⁷Montana State University, Bozeman, Montana 59717, USA
³⁸Moscow State University, Moscow, 119992, Russia

- ³⁹NASA/Goddard Space Flight Center, Greenbelt, Maryland 20771, USA
⁴⁰National Astronomical Observatory of Japan, Tokyo 181-8588, Japan
^{41a}Nikhef, Science Park, Amsterdam, the Netherlands
^{41b}VU University Amsterdam, De Boelelaan 1081, 1081 HV Amsterdam, the Netherlands
⁴²Northwestern University, Evanston, Illinois 60208, USA
^{43a}Université Nice-Sophia-Antipolis, CNRS, Observatoire de la Côte d'Azur, F-06304 Nice, France
^{43b}Institut de Physique de Rennes, CNRS, Université de Rennes 1, 35042 Rennes, France
^{44a}INFN, Gruppo Collegato di Trento, Italy
^{44b}Università di Trento, I-38050 Povo, Trento, Italy
^{44c}INFN, Sezione di Padova, Italy
^{44d}Università di Padova, I-35131 Padova, Italy
^{45a}IM-PAN, 00-956 Warsaw, Poland
^{45b}Warsaw University, 00-681 Warsaw, Poland
^{45c}Astronomical Observatory, Warsaw University, 00-478 Warsaw, Poland
^{45d}CAMK-PAN, 00-716 Warsaw, Poland
^{45e}Białystok University, 15-424 Białystok, Poland
^{45f}IPJ, 05-400 Świerk-Otwock, Poland
^{45g}Institute of Astronomy, 65-265 Zielona Góra, Poland
⁴⁶RMKI, H-1121 Budapest, Konkoly Thege Miklós út 29-33, Hungary
⁴⁷Rochester Institute of Technology, Rochester, New York 14623, USA
⁴⁸Rutherford Appleton Laboratory, HSIC, Chilton, Didcot, Oxon OX11 0QX United Kingdom
⁴⁹San Jose State University, San Jose, California 95192, USA
⁵⁰Sonoma State University, Rohnert Park, California 94928, USA
⁵¹Southeastern Louisiana University, Hammond, Louisiana 70402, USA
⁵²Southern University and A&M College, Baton Rouge, Louisiana 70813, USA
⁵³Stanford University, Stanford, California 94305, USA
⁵⁴Syracuse University, Syracuse, New York 13244, USA
⁵⁵The Pennsylvania State University, University Park, Pennsylvania 16802, USA
⁵⁶The University of Melbourne, Parkville VIC 3010, Australia
⁵⁷The University of Mississippi, University, Mississippi 38677, USA
⁵⁸The University of Sheffield, Sheffield S10 2TN, United Kingdom
⁵⁹The University of Texas at Austin, Austin, Texas 78712, USA
⁶⁰The University of Texas at Brownsville and Texas Southmost College, Brownsville, Texas 78520, USA
⁶¹Trinity University, San Antonio, Texas 78212, USA
⁶²Tsinghua University, Beijing 100084 China
⁶³Universitat de les Illes Balears, E-07122 Palma de Mallorca, Spain
⁶⁴University of Adelaide, Adelaide, SA 5005, Australia
⁶⁵University of Birmingham, Birmingham, B15 2TT, United Kingdom
⁶⁶University of Florida, Gainesville, Florida 32611, USA
⁶⁷University of Glasgow, Glasgow, G12 8QQ, United Kingdom
⁶⁸University of Maryland, College Park, Maryland 20742, USA
⁶⁹University of Massachusetts, Amherst, Amherst, Massachusetts 01003, USA
⁷⁰University of Michigan, Ann Arbor, Michigan 48109, USA
⁷¹University of Minnesota, Minneapolis, Minnesota 55455, USA
⁷²University of Oregon, Eugene, Oregon 97403, USA
⁷³University of Rochester, Rochester, New York 14627, USA
⁷⁴University of Salerno, I-84084 Fisciano (Salerno), Italy and INFN (Sezione di Napoli), Italy
⁷⁵University of Sannio at Benevento, I-82100 Benevento, Italy and INFN (Sezione di Napoli), Italy
⁷⁶University of Southampton, Southampton, SO17 1BJ, United Kingdom
⁷⁷University of Strathclyde, Glasgow, G1 1XQ, United Kingdom
⁷⁸University of Western Australia, Crawley, WA 6009, Australia
⁷⁹University of Wisconsin–Milwaukee, Milwaukee, Wisconsin 53201, USA
⁸⁰Washington State University, Pullman, Washington 99164, USA

(Received 8 March 2011; published 6 June 2011; corrected 12 April 2012)

We present the first modeled search for gravitational waves using the complete binary black-hole gravitational waveform from inspiral through the merger and ringdown for binaries with negligible component spin. We searched approximately 2 years of LIGO data, taken between November 2005 and September 2007, for systems with component masses of 1–99 M_{\odot} and total masses of 25–100 M_{\odot} . We did not detect any plausible gravitational-wave signals but we do place upper limits on the merger rate of

binary black holes as a function of the component masses in this range. We constrain the rate of mergers for $19M_{\odot} \leq m_1, m_2 \leq 28M_{\odot}$ binary black-hole systems with negligible spin to be no more than $2.0 \text{ Mpc}^{-3} \text{ Myr}^{-1}$ at 90% confidence.

DOI: [10.1103/PhysRevD.83.122005](https://doi.org/10.1103/PhysRevD.83.122005)

PACS numbers: 95.85.Sz, 04.80.Nn, 07.05.Kf, 97.60.Jd

I. INTRODUCTION

This paper presents a search for gravitational waves from binary black-hole (BBH) coalescences with total mass $25M_{\odot} \leq M \leq 100M_{\odot}$ and component masses $1M_{\odot} \leq m_1, m_2 \leq 99M_{\odot}$. The search used Laser Interferometer Gravitational-wave Observatory (LIGO) [1] data taken during the fifth science run (S5) from November 2005 to September 2007, when both LIGO sites were operating. The first LIGO site in Hanford, Washington hosts two interferometric gravitational-wave detectors, a 4 km detector, H1, and a 2 km detector, H2. The second site in Livingston, Louisiana hosts a single 4 km detector, L1. The Virgo detector [2] in Cascina, Italy commenced its first science run (VSR1) on May 18, 2007, and since then, LIGO and Virgo have operated their instruments as a network. However, this search did not use Virgo data, because it was not as sensitive to these high-mass systems during VSR1. Additionally, the GEO600 detector in Germany was functioning during S5. However, GEO600 data was not analyzed for similar reasons. The search results for compact binaries with total mass $M \leq 35M_{\odot}$ in LIGO S5 and Virgo VSR1 data have been reported in [3–5]. To date, no gravitational waves have been directly observed.

The gravitational-wave driven evolution of BBHs is conventionally split into three stages—inspiral, merger, and ringdown (IMR). The gravitational-wave signal during the adiabatic inspiral phase can be described by post-Newtonian (PN) expansion (see e.g., [6,7]). This technique is very accurate for comparable-mass systems at large separations, but grows less accurate as the merger is approached, eventually breaking down completely near the innermost stable circular orbit (ISCO) [8]. Modeling of the merger requires the numerical solution of the full Einstein equations in a highly dynamical strong-field regime. After the merger, the rapidly damped quasinormal ringdown of the black hole (BH) toward a stationary Kerr black hole is described by black-hole perturbation theory. This is the first analysis that incorporates a template family of waveforms modeling all three stages of BBH coalescence. This search covers systems for which the effects of BH spins can be neglected for detection. For BHs in this mass range the merger occurs in the LIGO detectors' most sensitive frequency band.

A. Motivation to search for higher mass systems

Black holes observed in X-ray binaries range up to $\sim 20M_{\odot}$ [9–12], and predictions from population-synthesis

models have typically suggested the masses of components of BH-BH binaries that merge within 10 Gyr will mostly lie in the range $5M_{\odot} \leq m_1, m_2 \leq 10M_{\odot}$ [13,14]. However, a number of channels have been suggested through which significantly more massive black-hole binaries could form.

Observations of IC10 X-1, a binary with a massive black hole ($\geq 24M_{\odot}$) accreting from a Wolf-Rayet companion star, and a similar recently observed binary NGC 300 X-1 [15], suggest that more massive BH-BH binaries can form through isolated binary evolution, with component masses $\sim 20M_{\odot}$ [16]. Meanwhile, several simulations over the past few years have indicated that dynamical formation could significantly contribute to coalescence rates involving BH-BH binaries in dense stellar environments, such as globular and nuclear star clusters [17–20]. The most massive black holes are likely to sink to the centers of clusters through mass segregation and substitute into binaries during three-body encounters, thus favoring relatively massive components in dynamically formed BH-BH binaries. Moreover, the BH merger products in such dense clusters can be reused if they are not ejected from the cluster due to recoil kicks, leading to higher-mass mergers in subsequent generations; component masses for BH-BH mergers in globular clusters can therefore range to $\sim 30M_{\odot}$ [18] and beyond. Additionally, although stellar winds in high-metallicity environments may prevent the formation of massive black holes, mass loss through stellar winds would be much less significant in low-metallicity environments, allowing more massive black holes to form [21,22].

Binaries, including an intermediate-mass black hole (IMBH) having a mass $50M_{\odot} \leq m \leq 500M_{\odot}$, could represent another exciting source for LIGO and Virgo detectors. Observational evidence for IMBHs is still under debate (see reviews [23,24] for additional details), although a recently discovered ultraluminous X-ray source [25] represents a possible IMBH detection. If IMBHs do exist in the centers of some globular clusters, they could contribute to coalescence rates in one of three ways: (i) through inspirals of stellar-mass compact objects into IMBHs [26,27]; (ii) through mergers of two IMBHs that formed in the same stellar cluster [28]; and (iii) through mergers of IMBHs from two different globular clusters when their host clusters merge [29]. It may also be possible to detect mergers of binary IMBHs arising from a direct collapse of early population III binary stars [30]. Although the rates of events involving IMBHs are highly uncertain, they may reach tens of detections per year in the Advanced LIGO/Virgo era (see [31] for a review of expected

detection rates for all binary types relevant to the advanced-detector era).

B. Complete inspiral, merger, and ringdown waveforms from numerical relativity

Constructing nonperturbative numerical solutions for the merger of two black holes has proven to be remarkably difficult. It has taken more than four decades since Hahn and Lindquist first attempted the numerical investigation of colliding black holes [32] to compute the gravitational-wave signal from the last orbits, merger, and ringdown of a black-hole binary system. These simulations are now possible using many different methods. Only months after Pretorius' initial breakthrough in 2005 [33], his success was repeated using a different approach [34,35], and since then several numerical relativity (NR) groups were able to produce increasingly accurate BBH simulations exploring increasing portions of the parameter space (see, e.g. [36–40] for recent overviews on the field, and Sec. 2 of [41] for a compact summary). The success of NR simulations has led to a range of new physical insights, including the calculation of recoil velocities produced by asymmetric emission of gravitational radiation during the merger process [42–60] and the prediction of the parameters of the remnant Kerr BH for a wide class of initial configurations [44,61–66,66–74]. Most importantly for the gravitational wave (GW) community, these simulations were able to compute accurate GW waveforms from the late inspiral and merger of BBHs in many configurations. The Samurai project [75] demonstrated the consistency of waveforms produced by different numerical codes. The waveforms predicted by these simulations have been successfully matched to PN and effective one-body (EOB) predictions [76–95]. Thus, by combining analytical and numerical calculations, it is now possible to construct accurate waveform templates coherently modeling the IMR of the coalescence of BBHs, as described in Sec. II.

In addition to the above, the signal waveforms generated by numerical simulations have begun to be directly used in testing data analysis pipelines. In particular, the NINJA project [41,96] tested the performance of a number of data analysis pipelines on data sets containing injections of numerically-simulated waveforms into colored Gaussian noise.

C. Summary of past searches

The LIGO and Virgo Scientific collaborations previously searched for systems that are a subset of the BBH parameter space explored by this analysis using different techniques. Previous searches used templates that modeled only the inspiral or ringdown phases. None employed templates that include IMR waveforms.

The first inspiral search explored systems with component masses in the range $3M_{\odot} \leq m_1, m_2 \leq 20M_{\odot}$ in ~ 386 hours of LIGO's second science (S2) run [97] with a 90%

sensitivity to systems up to 1 Mpc. The second inspiral search covered sources up to $40M_{\odot}$ total mass for LIGO's third science run (S3, 788 hours) and up to $80M_{\odot}$ in total mass for the fourth science run (S4, 576 hours) [98] with ~ 10 times the range sensitivity of S2, and placed a 90% confidence upper limit on the merger rate of $\sim 0.3L_{10}^{-1} \text{ yr}^{-1}$ for systems with a total mass of $\sim 40M_{\odot}$. (Here, L_{10} is 10^{10} times the blue Solar luminosity and is used as a proxy for the expected number of sources in a galaxy. For searches that extend beyond ~ 20 Mpc, there are approximately $0.0198L_{10} \text{ Mpc}^{-3}$ [99]. The presently discussed search extends beyond 20 Mpc and has sufficient sensitivity to use units of $\text{Mpc}^{-3} \text{ Myr}^{-1}$. Additionally, the Milky Way is $\sim 1.7L_{10}$.) The S2, S3, and S4 science runs used phenomenological waveforms proposed by [100] that extended the inspiral to higher frequency but did not include the complete IMR signal nor the effects of spin. A search that used templates including the spin effects was conducted over S3 data targeting asymmetric systems with component masses $1M_{\odot} \leq m_1 \leq 3M_{\odot}$ and $12M_{\odot} \leq m_2 \leq 20M_{\odot}$ [101].

BBH mergers with sufficiently high mass will have most of their in-band gravitational-wave amplitude in the ringdown phase. A search over S4 data probed the ringdown phase of BBH coalescence and placed 90% confidence upper limits on the merger rate for systems with total masses $85M_{\odot} \leq M \leq 390M_{\odot}$ of $1.6 \times 10^{-3} L_{10}^{-1} \text{ yr}^{-1}$ ($32 \text{ Mpc}^{-3} \text{ Myr}^{-1}$) [102]. The ringdown waveforms are a function of the final state of the black hole and do not depend on the details of the merger. For this reason, a spectrum of initial states (arbitrary spins and component masses) can be probed via a ringdown-only search.

Finally, the LIGO Scientific Collaboration (LSC) and Virgo searched S5 data and Virgo's first science run data (VSR1, which overlapped with the last ~ 6 months of S5) for BBHs with a total mass up to $35M_{\odot}$ [3–5]. The 90% confidence upper limit on merger rate for black hole binaries with total mass $\sim 30M_{\odot}$ was $\sim 3 \times 10^{-4} L_{10}^{-1} \text{ yr}^{-1}$, which is $\sim 6 \text{ Mpc}^{-3} \text{ Myr}^{-1}$ [5].

D. Summary of the present results

No plausible gravitational-wave signals were detected in this search. The loudest events are discussed in Sec. IV. Despite not detecting BBH signals directly, we are able to infer an upper limit on the merger rate of such systems in the nearby Universe. We do not impose a particular population model within our mass range and instead present our merger rate limits as a function of component mass ranges. To 90% confidence we constrain the rate of mergers for $19M_{\odot} \leq m_1, m_2 \leq 28M_{\odot}$ binary black hole systems to be no more than $2.0 \text{ Mpc}^{-3} \text{ Myr}^{-1}$. We highlight numbers from this range because it may include some of the heavier BH binaries that may arise in population-synthesis models (e.g., [22]), but was not covered by the S5 low-mass search [3–5]. Additional mass pair rate limits are given in Sec. V.

The paper organization is as follows. In Sec. II, we describe two families of waveforms used in this search (effective one-body model and phenomenological IMR model). Section III summarizes the key points of our data analysis pipeline. This part includes information about the template bank, data quality, background estimation, and candidate ranking statistics. Section IV contains results of the search; in particular, we present the loudest events. In Sec. V, we discuss detection efficiency, which we estimate by injecting simulated signals into the detector data. Additionally in this section, we present an upper limit on the coalescence rate for this search. Finally, Sec. VI presents the conclusions and plans for future improvements.

II. WAVEFORMS USED IN THIS SEARCH

Modeled waveforms are invaluable tools for extracting weak signals from noisy data in gravitational-wave searches for compact binaries [103]. The models are used to efficiently filter the data for signals and to assess the sensitivity of the instruments and data analysis procedure via simulations. This section motivates the need for new waveform models in this search and describes the models chosen.

For binaries with a total mass in the range targeted by this search, $25\text{--}100M_{\odot}$, the ISCO is reached in the sensitive frequency band of the LIGO interferometers. Thus, standard inspiral-only PN waveforms, which are typically terminated at the ISCO frequency, do not capture all of the observable signal. Furthermore, this abrupt, in-band end of the search templates can be problematic for the signal consistency checks. On the other hand, IMR templates model all of the observable signal and naturally decay away during the ringdown phase rather than abruptly ending. For these reasons, it is highly desirable to use IMR template waveforms to search for binary coalescences in this mass range. In Fig. 1, we plot an example IMR waveform in the time and frequency domains and note the extra signal relative to inspiral-only waveforms.

Fortunately, the recent breakthroughs in numerical relativity (see Sec. IB) have revealed the nature of the merger and ringdown phases of BBH coalescences. While it is infeasible to use the NR simulations directly as search templates, insights gained from the simulations have informed the development of analytic IMR waveform models. Currently, two main paradigms exist in the construction of IMR waveforms. In the EOB approach, an effective-one-body description of the two-body problem is tuned with NR simulations and then matched to the quasinormal modes of the BH ringdowns to produce analytical IMR waveforms in the time domain. In the phenomenological IMR model, the NR waveforms are matched to PN waveforms to produce “hybrid” PN-NR waveforms, which are then parametrized to produce analytical IMR templates in the frequency domain. Both EOB

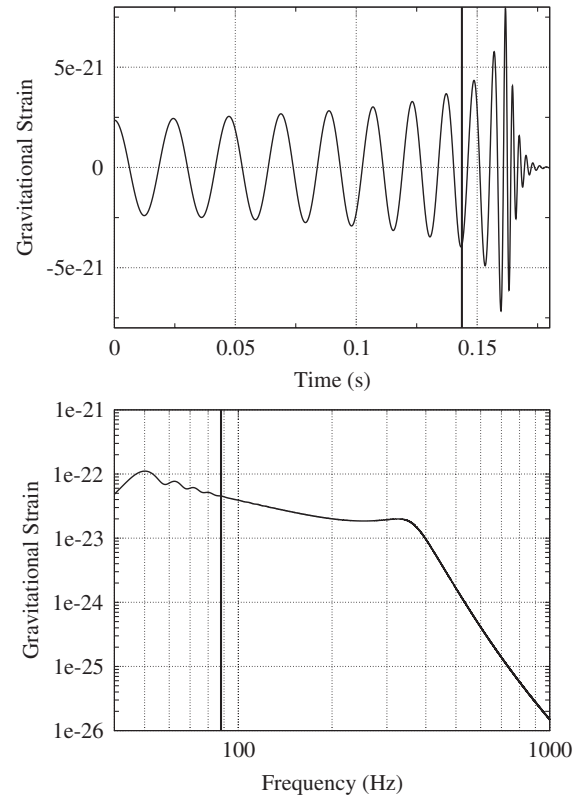


FIG. 1. Example of the *EOBNRv1* IMR waveforms used in this search for a $(25 + 25)M_{\odot}$ binary optimally located and oriented at 100 Mpc in the time domain (top panel) and the frequency domain (bottom panel). The solid vertical lines mark the location of the Schwarzschild ISCO, which is the termination point for inspiral-only waveforms. The oscillations appearing in the template $\tilde{h}(f)$ at low frequencies are due to the abrupt start of the time-domain waveform. However, the detectors have very little sensitivity at these frequencies, and so these oscillations have a negligible effect on the matched filter output.

and phenomenological IMR waveforms build on PN results [104–107]. The EOB waveforms are used as search templates and also as injected waveforms to test our detection efficiency. The phenomenological waveforms are used for injections and provide a check that our search pipeline can detect waveforms which are slightly different than our search templates. The next two subsections describe each of these families of analytic IMR waveforms.

Since EOB waveforms are generated in the time domain, the presence of an abrupt starting point at a given low frequency can result in spurious high frequency power. To mitigate these effects, a tapering window was applied to the beginning of the generated EOB waveforms [108].

A. Effective one-body model

The EOB approach, originally introduced in [109,110], provides a PN-resummed Hamiltonian, which can be used to evolve a binary system through its inspiral and the final “plunge” of the compact objects before they merge. This

trajectory can be used to generate a waveform $h^{\text{insp-plunge}}(t)$, which can be matched onto a waveform $h^{\text{merger-RD}}(t)$ describing the merger and ringdown of the resulting black hole, made up of a superposition of the black hole's quasinormal modes. The two pieces are combined at a suitably chosen matching time t_{match} to produce an inspiral-plunge merger-ringdown EOB waveform [110]

$$h(t) = h^{\text{insp-plunge}}(t)\Theta(t_{\text{match}} - t) + h^{\text{merger-RD}}\Theta(t - t_{\text{match}}), \quad (2.1)$$

where $\Theta()$ is the Heaviside step function.

The inspiral-plunge EOB waveform at leading-order amplitude in a PN expansion is determined from the trajectory $r(t)$, $\phi(t)$ as [110]

$$h^{\text{insp-plunge}}(t) \equiv \frac{4GM\eta}{D_L c^2} \left(\frac{GM}{c^3} \frac{d\phi}{dt} \right)^{2/3} \cos[2\phi(t)], \quad (2.2)$$

where D_L is the luminosity distance. We now summarize the fundamentals of the EOB calculation of the trajectory; more details can be found in [85–92,109–112]. As usual, m_1 and m_2 are the black hole masses, $M = m_1 + m_2$ is the total mass of the binary, $\mu = m_1 m_2 / M$ is the reduced mass, and $\eta = \mu / M$ is the symmetric mass ratio.

For a binary with negligible spin effects, the motion is confined to a plane and can be described in the center of mass by polar coordinates (r, ϕ) . The conservative dynamics is then captured by a Hamiltonian $H^{\text{EOB}}(r, p_r, p_\phi)$. The trajectory is evolved according to Hamilton's equations [110]

$$\frac{dr}{dt} = \frac{\partial H^{\text{EOB}}}{\partial p_r}(r, p_r, p_\phi), \quad (2.3a)$$

$$\frac{d\phi}{dt} = \frac{\partial H^{\text{EOB}}}{\partial p_\phi}(r, p_r, p_\phi), \quad (2.3b)$$

$$\frac{dp_r}{dt} = -\frac{\partial H^{\text{EOB}}}{\partial r}(r, p_r, p_\phi), \quad (2.3c)$$

$$\frac{dp_\phi}{dt} = \mathcal{F}_\phi(r, p_r, p_\phi). \quad (2.3d)$$

The inspiral of the binary comes about due to the addition of nonconservative dynamics in the last of Hamilton's equations via the tangential radiation-reaction force \mathcal{F}_ϕ arising from the basic PN expression of the energy flux. Here, we use a Keplerian Padé resummation [113] of the energy flux as given by Eq. (15) of [87]. More recent models have used more sophisticated fluxes, such as the ρ -resummation [114] and non-Keplerian flux models which describe non-quasi-circular effects [88,89,91,92].

The form of the EOB (resummed) Hamiltonian is [109]

$$H^{\text{EOB}}(r, p_r, p_\phi) = Mc^2 \sqrt{1 + 2\eta \left(\frac{H^{\text{eff}}}{\mu c^2} - 1 \right)}, \quad (2.4)$$

where H^{eff} is the effective Hamiltonian [109,111]

$$H^{\text{eff}} = \mu c^2 \left(A(r) \left[1 + \frac{A(r)}{D(r)} \frac{p_r^2}{M^2 c^2} + \frac{p_\phi^2}{M^2 c^2 r^2} + 2(4 - 3\eta)\eta \frac{G^2 p_r^4}{M^2 c^8 r^2} \right] \right)^{1/2} \quad (2.5)$$

and where the radial potential functions $A(r)$ and $D(r)$ appear in the effective metric [109]

$$ds_{\text{eff}}^2 = -A(r)c^2 dt^2 + \frac{D(r)}{A(r)} dr^2 + r^2(d\theta^2 + \sin^2\theta d\phi^2). \quad (2.6)$$

The Taylor-approximants to the coefficients $A(r)$ and $D(r)$ can be written as

$$A_k(r) = \sum_{i=0}^{k+1} a_i(\eta) \left(\frac{GM}{rc^2} \right)^i, \quad (2.7a)$$

$$D_k(r) = \sum_{i=0}^k d_i(\eta) \left(\frac{GM}{rc^2} \right)^i. \quad (2.7b)$$

The functions $A(r)$, $D(r)$, $A_k(r)$ and $D_k(r)$ all depend on the symmetric mass ratio η through the η -dependent coefficients $a_i(\eta)$ and $d_i(\eta)$. [When $\eta \rightarrow 0$, $A(r) \rightarrow 1 - \frac{2GM}{rc^2}$ and $D(r) \rightarrow 1$ and the metric (2.6) reduces to the Schwarzschild metric.] These coefficients are currently known through 3PN order (i.e., up to $k = 3$) and can be found in [87]. During the last stages of inspiral and plunge, the EOB dynamics can be adjusted closer to the numerical simulations by including in the radial potential $A(r)$ a pseudo 4PN coefficient $a_5(\eta) = a_5 \eta$, with a_5 a constant. Here, we follow [87] and fix $a_5 = 60$. We refer to this model, the first NR-adjusted EOB model implemented for a search of GW data, as *EOBNRv1*. Since [87] was published, more accurate numerical simulations became available and more sophisticated EOB models have been calibrated. This includes a different value of a_5 , and also the introduction of a pseudo 5PN coefficient $a_6(\eta) = a_6 \eta$ [91], with a_6 a constant. We refer to the second NR-adjusted EOB model implemented for a search of GW data, as *EOBNRv2*. This most recent EOB template family has been developed in [115]; it includes the latest improvements [88–90,92] to the EOB model and also other refinements which are necessary to match highly-accurate NR waveforms for a broad range of mass ratios.

In order to assure the presence of a horizon in the effective metric (2.6), a zero needs to be factored out from $A(r)$. This is obtained by applying a Padé resummation [111]. The Padé resummations of $A(r)$ and $D(r)$ at pseudo 4PN order are denoted $A_4^1(r)$ and $D_4^0(r)$ [116], and the explicit form used in this paper can be read from [87].

The merger-ringdown waveform in the EOB approach is built as a superposition of quasinormal modes, [85,110,117]

$$h^{\text{merger-RD}}(t) = \sum_{n=0}^{N-1} A_n e^{-i\sigma_n(t-t_{\text{match}})}, \quad (2.8)$$

where n is the overtone number of the Kerr quasinormal mode, N is the number of overtones included in our model, and A_n are complex amplitudes to be determined by a matching procedure described below. We define $\sigma_n \equiv \omega_n - i\alpha_n$, where the oscillation frequencies $\omega_n > 0$ and the inverse decay-times $\alpha_n > 0$, are numbers associated with each quasinormal mode. The complex frequencies are known functions, uniquely determined by the final black-hole mass and spin. They can be found in [118]. The final black-hole masses and spins are obtained from the fitting to numerical results worked out in [87].

The complex amplitudes A_n in Eq. (2.8) are determined by matching the EOB merger-ringdown waveform with the EOB inspiral-plunge waveform close to the EOB light ring. In particular, here we use the matching point, which is provided analytically by Eq. (37) of [87]. In order to do this, we need N independent complex equations that are obtained at the matching time by imposing continuity of the waveform and its time derivatives,

$$\frac{d^k}{dt^k} h^{\text{insp-plunge}}(t_{\text{match}}) = \frac{d^k}{dt^k} h^{\text{merger-RD}}(t_{\text{match}}), \quad (2.9)$$

$$A_{\text{eff}}(f) \equiv C \begin{cases} (f/f_{\text{merg}})^{-7/6} & f < f_{\text{merg}} \\ (f/f_{\text{merg}})^{-2/3} & f_{\text{merg}} \leq f < f_{\text{ring}} \\ w \mathcal{L}(f, f_{\text{ring}}, \sigma) & f_{\text{ring}} \leq f < f_{\text{cut}} \end{cases} \quad (2.10a)$$

$$\Psi_{\text{eff}}(f) \equiv \frac{1}{\eta} \sum_{k=0}^7 (x_k \eta^2 + y_k \eta + z_k) (\pi M f)^{(k-5)/3} + 2\pi f t_0 + \varphi_0. \quad (2.10b)$$

In the above expressions, C is a numerical constant whose value depends on the location and orientation of the binary as well as the physical parameters, $\mathcal{L}(f, f_{\text{ring}}, \sigma)$ is a Lorentzian function that has a width σ , and that is centered around the frequency f_{ring} . The normalization constant w is chosen so as to make $A_{\text{eff}}(f)$ continuous across the “transition” frequency f_{ring} . The parameter f_{merg} is the frequency at which the power-law changes from $f^{-7/6}$ to $f^{-2/3}$. The phenomenological parameters $\mu_j \equiv \{f_{\text{merg}}, f_{\text{ring}}, \sigma, f_{\text{cut}}\}$ are given in terms of the physical parameters of the binary as: $\pi M \mu_j = a_j \eta^2 + b_j \eta + c_j$. The coefficients $\{a_j, b_j, c_j | j = 0 \dots 3\}$ and $\{x_k, y_k, z_k | k = 0, 2, 3, 4, 6, 7\}$ are tabulated in Table I of [121]. We refer to the waveform family defined by these coefficients as *IMRPhenomA*, and these are the waveforms used for injections in the present search. These waveforms are generated in the frequency domain and are then converted to the time domain for injections by means of the inverse Fourier transform.

with $k = 0, 1, 2, \dots, N - 1$. In this paper, we use $N = 3$. The above matching approach is referred to as *point matching*. Although it gives better smoothness around the matching time, it is not very stable numerically when N is large and higher-order numerical derivatives are employed. More sophisticated matching procedures have been proposed in the literature to overcome the stability issue [88,89,91,92], and will be adopted in the future.

B. Phenomenological IMR model

Reference [119] presented a different way of constructing nonspinning IMR waveforms by combining PN calculations with numerical simulations. They first constructed a family of hybrid waveforms by matching PN waveforms with NR waveforms in certain overlapping time intervals where both the approaches are expected to be valid [93]. Restricted 3.5PN waveforms in the TaylorT1 approximation were matched to NR waveforms produced by the BAM NR code [120]. These hybrid waveforms were used to construct a family of analytical waveforms in the Fourier domain, of the form $\tilde{h}(f) \equiv A_{\text{eff}}(f) e^{i\Psi_{\text{eff}}(f)}$, where the effective amplitude and phase are expressed as:

The choice of the time interval for matching PN and NR waveforms is somewhat *ad hoc*. Currently, the matching interval is chosen so as to maximize the fit of PN and NR waveforms. Moreover, the PN waveforms employed in the matching are computed in the *restricted* PN approximation, and the amplitude of the NR waveforms is scaled to match with PN waveforms. This causes the amplitude of the waveforms to have a systematic bias of $\sim 10\%$. Later improvements in this model have already addressed some of these issues [94]; we refer to this improved waveform family as *IMRPhenomB*.

C. Systematic errors in waveform models

Although the two waveform families have been tested via comparisons to numerical waveforms, there are a number of possible sources of systematic uncertainty in the two waveform families. For example, as discussed above, there are subtleties in choosing the matching interval between PN inspiral waveforms and numerical simulations when

constructing the hybrid waveforms used to calibrate the Phenomenological waveforms. Similarly, the EOB procedure to attach the merger-ringdown waveform to the inspiral-plunge waveform can be quite delicate and become unstable if not done properly. Most notably, both waveform families have been tested against numerical simulations only in the nearly-equal-mass regime, up to ratios of 3:1 and 4:1. It is not clear whether these waveforms are faithful to the actual signals in the case of highly unequal masses.

The waveform models initially used for this search, *EOBNRv1* and *IMRPhenomA*, had both been revised by the time the search neared completion. The revisions, which included improved calibration and more accurate matching to NR waveforms, as well as improved modeling of the post-Newtonian inspiral phase, resulted in waveforms that were significantly more faithful. For example, the revised version of the phenomenological waveform family, *IMRPhenomB*, has systematic biases in SNR of $\leq 10\%$ relative to NR waveforms in the mass range of interest and for mass ratios below 4:1; for the revised version of the EOB waveform family, *EOBNRv2*, the systematic biases in SNR relative to NR waveforms are $\leq 3\%$. These systematic biases do not account for any errors in the NR waveforms themselves.

The largest effect of the revision of both models was to systematically reduce the gravitational-wave amplitude during merger. We found that within our errors, it was sufficient to adjust the distance of the simulated signals to take into account the lower intrinsic gravitational-wave amplitude in the corrected models. The upper limits quoted in Sec. V are thus based on a search carried out with *EOBNRv1* templates, but with the distances of *EOBNRv1* and *IMRPhenomA* injections adjusted to match the SNR of the revised *EOBNRv2* and *IMRPhenomB* waveform models.

We can get a sense of the systematic uncertainty in the waveform amplitudes by comparing the SNRs between the two waveform families. We find that the SNR of the most recent versions of the two families, *EOBNRv2* and *IMRPhenomB*, agrees to better than $\sim 10\%$ for mass ratios less than 6:1 in the mass range of interest, but diverges by nearly 50% for mass ratios of 10:1. The latter value is chosen as the limit on the mass ratio for phenomenological IMR injections.

III. THE DATA ANALYSIS PROCEDURE

The data analysis procedure involves a multistage pipeline that automates the extraction of signals from the data, the analysis of coincident events between detectors and the estimation of background. The pipeline used for this search was similar to that of previous S5 searches [3–5] except for the choice of template waveforms and some minor points described in subsequent sections.

Here, we summarize the data analysis procedure. First, data for the three different detectors, H1, H2, and L1 are

divided into 2048 s blocks in order to estimate the time dependent power spectral density (PSD) of the detector noise. The PSD is required to choose the search templates and to filter the data itself. Next, the data are processed in a two-stage procedure. The first stage filters the data with the templates and identifies potential events in each detector. Then the pipeline checks for coincidence between detectors. We allow double and triple coincident combinations between detectors. After finding coincident events, the data are refiltered using only the templates that participated in the coincident events. The data needs to be filtered with fewer templates at the second stage after demanding coincidence with other detectors. The second filtering stage employs the χ^2 veto [122], which drastically reduces the background of this search, but is too computationally expensive to be performed during the first filtering stage with the full template bank. Once coincident events are identified, they are clustered in a 10 s window to produce a maximum of one coincident event every ten seconds. We apply the same procedure to time-shifted data streams and compare the time-shifted results to the zero-lag results to assess the significance of our events. This procedure is repeated with simulated signals in order to assess the sensitivity of the pipeline.

In the remaining sections, we elaborate on this procedure, emphasizing differences with previously published searches.

A. Generation of coincident event candidates

In this section, we describe the process of obtaining candidate events. First, we discuss how to choose templates to filter the data. Next, we describe the filter process itself and how to identify events that are significant in a single-detector. We then describe how we check for coincident events between detectors. Finally, we describe how data quality impacts our assessment of candidates.

1. Selection of search template parameters

The observed gravitational waveform depends on the component masses of the binary. A bank of template waveforms called a template bank is chosen to adequately cover the parameter space of possible waveforms. The template bank used for the search consisted of templates covering total mass between $25\text{--}100M_{\odot}$, and component masses between $1\text{--}99M_{\odot}$. The bank was tiled using a hexagonal placement algorithm [123], such that the intended minimum SNR was 97% of its maximal value [124]. The template spacing was determined using the metric calculated for the stationary phase approximation [125,126] extended to the effective ringdown frequency. This metric, terminated at ISCO frequency, was used in previous searches for signals from low-mass systems. Although the metric is not formally correct for the EOB templates used in this search, it has been found that the bank provides the desired minimal match for most of the parameter space

and, at worst, a 95% match for the high-mass region of the bank. The average number of templates required to cover this parameter space was ~ 1600 per detector.

2. Filtering

After properly selecting the templates to cover the mass parameter space, the data are filtered. The signal to noise ratio for a given template waveform $h(t)$ is a convolution of the template with the data weighted by the noise power spectral density, defined as

$$z(t) = 4 \int_0^\infty \frac{\tilde{h}(f)^* \tilde{s}(f)}{S_n(f)} e^{2\pi i f t} df, \quad (3.1a)$$

$$\sigma^2 = 4 \int_0^\infty \frac{\tilde{h}(f)^* \tilde{h}(f)}{S_n(f)} df, \quad (3.1b)$$

where the tilde and $*$ denote a Fourier transform and a complex conjugate, s refers to the data, and S_n is the noise power spectral density. In order to cover the entire parameter space, all of the data are filtered with every template. $z(t)$ is a complex time series where the real part represents a template phase of 0 and the imaginary part represents a phase of $\pi/2$. The real-valued SNR ρ is given by $\rho(t) = |z(t)|/\sigma$.

We trigger on the local maxima of each filter's time series when the SNR is above 5.5, and record those times and template parameters. A list of triggers is then passed to the next stage of the pipeline, which checks for coincidence between detectors.

3. Coincidence test

We require events to be coincident in at least two detectors. For events to be considered coincident, the time of coalescence and the masses of the system [127] given by the triggers in each instrument must agree to within a certain tolerance [128]. Although we allowed for double coincident combinations, we discarded H2L1 events that lacked an H1 trigger if H1 was operating. Since H1 was more sensitive than H2 it should have produced a trigger for a real event.

As with the searches for low-mass compact binary coalescences in S5, we used a coincidence test based on the template bank metric. This test accounts for correlations between the different parameters and attains a lower false-alarm rate for a given detection efficiency than simple parameter cuts. As was noted earlier, the metric used in this search was suboptimal. To take into account this limitation, the coincidence requirements were looser than those of previous S5 searches [3–5].

4. Data quality vetoes

Not all of the data taken during S5 was used for this analysis. The detectors frequently lost lock or were taken out of lock for commissioning work. Only times with stable lock stretches deemed as analyzable were marked

as *science time*. Segments of *science time* containing more than 2048 s of data were analyzed in each of the three detectors H1, H2, L1.

Occasionally, data quality (DQ) during science time suffered from transient excess noise. Significant work was done to characterize these times prior to examining the search candidates so as to not bias our detection and upper limit statements [129]. Events at times suffering from poor data quality are removed from the analysis. The procedure of vetoing events reduces the live time and also the false-alarm rate of the search [129]. The following describes the basic procedure for vetoing candidates based on DQ.

The detectors are sensitive to a variety of noise transients (glitches) of nonastrophysical origin, such as instrumental glitches and environmental disturbances. The status of the detectors is monitored by a number of auxiliary data channels that record the internal degrees of freedom of the interferometers and the output from environmental sensors. When the status of a detector is suboptimal, the time is flagged. Because the templates used in this search have an impulse response lasting ~ 10 seconds, a short glitch can produce triggers lasting several seconds after the glitch occurs. DQ flag intervals often require search-specific time padding to improve the effectiveness of the flag. The length of this padding is determined by looking at the distribution of triggers in the flagged interval. The effectiveness of a DQ flag is evaluated by the following metrics: *Efficiency*: the percentage of single-detector triggers flagged. Because these triggers are analyzed before coincidence, they are dominated by transient noises local to the detector; *Dead-time*: the percentage of flagged time; *Used-percentage*: the fraction of flags that contain at least one background trigger. An effective flag has a high efficiency, a high used-percentage, and a low dead-time. Flags found to be effective by these metrics are used as vetoes.

DQ flags are classified into four veto categories, according to their metrics' performance. *Category 1* contains times when the data was not analyzed at all as described at the beginning of this section. *Category 2* includes vetoes with a high efficiency-to-dead-time ratio and a high used-percentage. The origin of these glitches is well-understood and time intervals are well-tuned. *Category 3* vetoes times with noise sources whose coupling with the gravitational-wave channel is less understood, such as those due to environmental noise. *Category 3* vetoes are less correlated with transients and are characterized by higher dead-time and lower used-percentage than category 2 vetoes. Some flags, for example, the overflows of digital channels monitoring the alignment of the interferometer arm lengths and mirrors, belong to both category 2 and 3 with different window lengths. *Category 4* contains vetoes with low efficiency and high dead-time. These flags usually identify minor environmental disturbances and problems recorded in the electronic logbooks.

TABLE I. The analyzed time surviving the pipeline after category 3 vetoes were applied. H1H2 times were not analyzed due to the inability to properly estimate the background for colocated detectors.

Detectors	Analyzed time (yr)
H1H2L1	0.6184
H1L1	0.0968
H2L1	0.0609

The DQ vetoes are used in the following way. Category 2 vetoes are used unconditionally in the search. We examine events after Category 2 for detection candidates. However, we apply Category 3 vetoes before creating the list of candidates used to constrain the BBH merger rate. The category 3 veto list is chosen in advance in order to not bias our rate limit results. Category 4 vetoes are used only to follow up interesting candidates; they do not have any impact on the rate limits quoted in this paper. All Category 2 or greater vetoes are applied after the second coincidence stage before clustering to produce the event list. Vetoes are accounted for to ensure that the analyzed time calculations are correct. Table I gives the analyzed time available after Category 3 vetoes are applied.

B. Ranking and evaluation of candidate events

1. Signal consistency check

Accounting for data quality as described in the previous section is not sufficient to remove all triggers caused by environmental or instrumental sources. For that reason, we employ a two-stage pipeline that performs an additional signal consistency check. In the second filtering stage we explicitly check the match of the signal to the template waveform by performing a chi-squared test [122]. In this test, the template is divided into p frequency bins (for this search, we use 10 bins) such that each bin contains the same expected contribution to the total SNR, if the signal matches the template exactly. The SNR of the trigger in each bin is compared to the expected SNR, and the differences are added in quadrature to obtain the value of χ^2 . We decompose the template waveforms into p pieces of identical power σ^2/p

$$\tilde{h}(f) = \sum_{i=1}^p \tilde{u}_i(f), \quad (3.2a)$$

$$\tilde{u}_i(f) = \tilde{h}(f)\Theta(f - f_{i,\text{low}})\Theta(f_{i,\text{high}} - f). \quad (3.2b)$$

Using (3.1a) we compute a filter time series for each of the orthogonal pieces.

$$z_i(t) = 4 \int_0^\infty \frac{\tilde{u}_i(f)^* \tilde{s}(f)}{S_n(f)} e^{2\pi i f t} df. \quad (3.3)$$

The χ^2 statistic is then computed as

$$\chi^2(t) = \frac{1}{\sigma} \sum_{i=1}^p \left| \frac{z_i(t)}{p} - z_i(t) \right|^2. \quad (3.4)$$

Since $z_i(t)$ is a complex number, corresponding to both phases of the filter, the χ^2 statistic has $2(p-1)$ degrees of freedom.

Previous searches in this mass range did not use IMR waveforms. Since the models were not accurate, they did not use a χ^2 test [98]. The χ^2 statistic already provides significant separation from noise for a large fraction of simulated signals in this search. Future search efforts in this mass range might employ new signal-based vetoes and multivariate classifiers to achieve a better separation of signal from background [130].

Once the χ^2 statistic is evaluated, we have almost all of the information necessary to begin ranking events. We describe in Sec. III B 3 how the χ^2 statistic is folded together with the SNR to produce a ranking statistic known as effective SNR. First, however, in Sec. III B 2, we describe how we estimate our background, which is also required for ranking the coincident events.

2. Background estimation

We assume that instrumental noise triggers are not correlated between detectors. We estimate the background of this search by examining accidental coincidences from time-shifted data. This section describes how we estimate the background. The next section describes how the background estimate is used in ranking events.

In order to estimate the background of coincident events, we repeat the coincidence analysis with 100 time shifts between the two LIGO sites in multiples of five seconds. We call the events found by this procedure time-slide events. We expect that there will be no correlated noise between the sites. Therefore, the time-shifted analysis provides 100 background trials to which we then compare the unshifted data. Unfortunately, the assumption of uncorrelated noise was not adequate for the colocated Hanford detectors, H1 and H2. All events found in H1 and H2 but not L1 were discarded due to correlated noise corrupting the background estimate.

We find that the estimated background of the search is a function of time, the parameters of the signals searched for, and which detectors observed the event. The total mass of the recovered signal is the best single parameter that tracked the signal parameter dependence of the time slides. We elaborate in Sec. III B 3 how this was used in the ranking of candidate events.

3. Ranking events

The ranking of candidate events is a multistage process. The end ranking statistic is a false-alarm rate (FAR) for each event that indicates how often events like it (or louder than it) occur in time slides. This section describes how we compute the FAR and rank our events.

First, single-detector triggers are assigned an *effective* SNR ρ_{eff} which is a function of ρ and χ^2 . The functional form is chosen to match the false-alarm rate contours of the single-detector background in the SNR— χ^2 plane. The effective SNR is defined as

$$\rho_{\text{eff}} = \frac{\rho}{[(1 + \rho^2/50)(\chi^2/\chi_{\text{dof}}^2)]^{1/4}}, \quad (3.5)$$

where 50 is an empirically determined parameter and $\chi_{\text{dof}}^2 = 2(p - 1)$ is 18 for this search. The single-detector effective SNRs $\rho_{\text{eff},i}$ are combined in quadrature to give a coincident effective SNR

$$\rho_{\text{eff},c} = \sqrt{\sum_i \rho_{\text{eff},i}^2}. \quad (3.6)$$

We compute the FAR by comparing the unshifted events to the time-slide events. Because of the non-Gaussian properties of the detector noise, the FAR depends on the template. It also depends on how many detectors were operating and participated in the event. We compute the FAR as a discrete function of four parameters, the total mass M , the detectors that participate in the coincidence P , the detectors that were functioning but not vetoed at the time of the coincidence F , and the combined effective SNR rank of the event R . We will denote a time-slide event that estimates our background as B . Each parameter is an index for the event B . The first and second indices, F and P , describe the instruments that were functioning during the event and the detectors that participated in the event. Only the following combinations were considered: 1) triggers found in H1 and L1 when only the H1 and L1 detectors were operating; 2) triggers found in H1 and L1 when all three detectors H1, H2 and L1 were operating; 3) triggers found in H2 and L1 when only H2 and L1 were operating; and 4) triggers found in all three detectors when all three detectors were operating. Note that as mentioned previously, we were not able to estimate a reliable background for triggers found only in H1 and H2. Therefore, those events were discarded. We also discarded events found in H2 and L1 when all three detectors were on since the more sensitive H1 should observe a real signal. To summarize, the following shorthand notation for the 4 combinations of participating P and functioning F detectors will be used: $P, F \in \{\text{H1L1}, \text{H1L1}; \text{H1L1}, \text{H1H2L1}; \text{H2L1}, \text{H2L1}; \text{H1H2L1}, \text{H1H2L1}\}$. The third index M denotes a range for the total mass estimated for the event and is in the set $\{[25, 50), [50, 85), [85, 100)\}M_{\odot}$. The fourth index R is the rank of the event given by its effective SNR, $\rho_{\text{eff},c}$. The R index is determined by assigning the event having a given P, F and M with the lowest combined effective SNR defined in (3.6) the value 0, and the next lowest 1, etc., until all events are ranked. We calculate the false-alarm rate FAR for a given event as the number of all time-slide events, B , with a rank (R^+) larger than that event's rank divided by the time analyzed T_F in the time-shifted

analyses, which is a only a function of the instruments that were on and not vetoed,

$$\text{FAR}_{PFMR} = \sum_{R^+ > R} B_{PFMR} + T_F^{-1}. \quad (3.7)$$

This now allows us to map a zero-lag (unshifted) event to a FAR by assigning it the same four parameters.

In addition to the indices describing how the false-alarm rate was computed, there is one remaining implicit parameter that refers to the time of the events. We separated the two calendar years of data into 12 two-month periods. Each was treated separately for the calculation of (3.7) in order to crudely capture the variation of the noise properties over the course of S5. It is worth making explicit the number of combinations over which false-alarm rates were computed. Each of the 12 two-month periods had 4 possible combinations of detectors that were functioning and that produced triggers as mentioned above. Additionally, each had 3 total mass bins. The result is $12 \times 4 \times 3 = 144$ separate calculations of (3.7). This is described additionally in Table II and is relevant for interpreting the significance of events in Sec. IV.

Next, we assess the FAR of the events independently of the mass range M and the participating detectors P in order to compute a global ranking that only takes into account the detectors that were functioning and no other parameters. To do this, we use the inverse FAR^{-1} as an intermediate ranking statistic to replace combined effective SNR as the rank in the index R . We denote these newly ranked time-slide events as B' . Then the combined FAR is

TABLE II. Breakdown of the analysis time and coincident trigger sets. The LIGO S5 run is divided into 12 epochs, each roughly two months in duration; within each epoch, the time is divided according to which detectors were operating and not vetoed. Since there are three allowed combinations of functioning detectors, there are $12 \times 3 = 36$ different analyzed time periods. Different combinations of coincident events are allowed, depending on which detectors are functioning and participated in the coincident event. There are a total of four possible functioning/participating detector combinations which contribute to the analysis. Within each observation epoch and functioning/participating detector combination, the events are divided into three mass bins according to the average total mass of the templates involved in the coincident event. This means there are a total of $12 \times 4 \times 3 = 144$ different types of coincident events. Each type of event has a separate background distribution used to calculate its false-alarm probability.

Observation	Detectors	Detectors	Mass
Epoch	Functioning, F	Participating, P	Range, M
12 ~ two-month	H1L1	H1L1	$[25, 50)M_{\odot}$,
epochs	H2L1	H2L1	$[50, 85)M_{\odot}$,
	H1H2L1	H1H2L1	and
		H1L1	$[85, 100]M_{\odot}$

$$\text{FAR}_{FR} = \sum_{R^+ > R} \sum_P \sum_M B'_{PFMR^+} T_F^{-1}. \quad (3.8)$$

The combined FAR is only a function of the detectors that were functioning F during the event, and the inverse FAR rank computed at the previous step R . From the combined FAR we can also compute the False-Alarm Probability (FAP). Assuming Poisson statistics, we define the FAP as the chance of getting one or more events louder than the event in question purely from background. This is defined as $\text{FAP}_{FR} = 1 - \exp(-\text{FAR}_{FR} T_F)$. T_F is nominally a particular detector combination live time for a two-month analysis period, but can be replaced with the entire observation time in order to obtain the FAP for an event given the result of all 12 two-month periods.

IV. LOUDEST COINCIDENT EVENTS

As previously mentioned, we divided the ~ 2 calendar years of data into 12 two-month blocks and this resulted in 144 separate computations of (3.7). Combining the FAR using (3.8) resulted in 36 separate periods consisting of distinct times when a given set of detectors were functioning and providing data. These categories are independent since they arise from distinct times. Since a lower FAR implies a more significant event, we use FAR^{-1} to rank the events.

Table III gives the top 10 loudest events of the search ranked by FAR^{-1} . Three of the 10 candidates were louder than any events in the 100 time-shifted coincident sets used to estimate the background. The table provides the bound on the FAR based on the total observed background time during their two-month period when the same detectors were functioning. We note that it is not surprising to have events louder than the background given the limitations of the background estimation. We used only 100 time shifts, and the number of trials examined for the computation of the FAR was 144. We, therefore, expected to observe ~ 1.4 events more significant than our estimated background and

we observed three. In order to estimate the significance of these three events, we employed two additional techniques. As the primary method, we first interpolated and extrapolated the FAR from our 100 time-shift background estimate. To obtain an alternative estimate, we extended our time-shift study to 1000 shifts for the two-month periods in which those events occurred. We decided before unblinding the analysis to use the extrapolated FAR values in the upper limit computation when necessary. We also examined many properties of these events in a qualitative follow-up procedure. The result of our analysis is that all three events have FAPs of $> 10^{-2}$, assuming the full 0.8 yr. observation time, and all are consistent with rare instrumental noise fluctuations; none are plausible candidate gravitational-wave detections. This section provides some additional detail about these events.

A. H1H2L1 event at GPS time 848905672.3369 (November 30, 2006 07:07:38.3369 GMT)

The loudest event of this search at GPS time 848905672.3369 was found in all three detectors and was more significant than any of the time-shifted events in its background estimate. We put a bound on its FAR from the original 100 time-shift background estimate of 1 per 5 years. We also estimated the FAR by interpolating and extrapolating the original 100 time-shift background estimate using a fit to the trigger distribution. The extrapolated FAR was 1/1.6 yr. Note that it was larger than the bound due to the fitting procedure in the tail of the trigger distribution. Also note that we decided in advance to use the extrapolated FARs for the rate limit calculations in the next section. Therefore, the FAR used for this event was 1/1.6 yr. We computed 1000 additional time shifts in this two-month period to better estimate its false-alarm probability. From the additional time-shift background estimate, we computed that this event had a false-alarm rate of 1/50 yr.

TABLE III. The loudest events of the search. The coincident events are ranked by their combined false alarm rate FAR. A “ - ” represents that the detector was not functioning during the time of the event in question. A “ * ” represents that the detector was functioning but did not produce a trigger above the single-detector SNR threshold of 5.5. Notice that the top three events were found above their local background estimates. For that reason, only limits on their combined FARs are given here. See the text for details.

Rank	FAR (yr ⁻¹)	ρ_{eff}	GPS Time	ρ_{H1}	χ_{H1}^2	m_{1H1}	m_{2H1}	ρ_{H2}	χ_{H2}^2	m_{1H2}	m_{2H2}	ρ_{L1}	χ_{L1}^2	m_{1L1}	m_{2L1}
1	<0.20	12.8	848905672.3369	172.0	4057.9	94.0	6.0	24.4	167.4	49.7	17.3	8.3	46.0	95.2	4.8
2	<0.25	11.6	825664840.1523	5.6	21.5	51.7	1.1	6.2	1.6	50.5	1.1	5.5	39.1	36.2	2.4
3	<1.40	10.3	842749918.8057	-	-	-	-	5.5	7.8	67.1	2.5	12.2	20.4	83.2	16.8
4	2.7	12.0	830222610.4062	5.5	34.2	98.0	2.0	*	*	*	*	28.8	43.5	91.7	8.3
5	5.4	9.8	849056023.4121	5.7	11.3	29.9	1.3	*	*	*	*	5.6	2.5	23.6	1.8
6	9.0	9.8	827865922.1265	9.2	67.6	37.3	1.2	-	-	-	-	6.8	4.2	31.0	1.5
7	12	9.5	836048263.0366	6.2	15.0	52.9	1.4	6.4	14.6	46.7	1.6	5.9	21.3	53.0	1.3
8	12	10.7	854487078.6543	6.1	29.6	96.7	3.3	*	*	*	*	18.1	29.8	97.0	3.0
9	13	10.8	835998008.6890	23.2	52.3	94.8	5.2	*	*	*	*	5.8	21.2	78.1	1.2
10	15	9.8	857817894.5767	8.8	29.7	90.7	1.4	9.9	40.8	94.8	5.2	5.9	28.1	90.4	1.4

Given that we searched nearly 1 year of data, this event is consistent with fluctuations. The conservative probability of getting this event in background (by choosing the lowest of the FAR estimates) is ~ 0.02 . Our assessment of this candidate is that it is a loud glitch in H1 with a moderate response in H2 coincident with low amplitude noise in L1. The ratio of distance estimates associated with the signals in H1 and H2 [132] is not consistent with a signal. We measured a ratio of ~ 10 and it should be ~ 1 . The H1 χ^2 does not lie within the expected signal distribution. We therefore conclude that this is not a gravitational-wave detection candidate.

B. H1H2L1 event at GPS time 825664840.1523 (March 06, 2006 07:20:26.1523 GMT)

The second loudest event of this search at GPS time 825664840.1523 was more significant than any of the 100 time slides performed during the two-month period in triple coincident H1,H2,L1 time. The event was found in all three detectors H1, H2, and L1, with SNR only slightly above threshold 5.60, 6.17 and 5.55, respectively. The masses were consistent between the detectors. In H1 and L1, this event had a χ^2 that was consistent with both time-slide events and signals. However, it had an unusually low χ^2 value (0.1 per degree of freedom) in H2. A χ^2 value of less than 0.1 per degree of freedom is rare for both signals and noise. No background events out of $\sim 300,000$ had such a low χ^2 value nor did any of the $\sim 10^6$ simulated signals. The ranking of this event was artificially elevated by the unusually low χ^2 value. If this event had a higher χ^2 of 1 per degree of freedom it would not stand above background. We conclude that this event is not a gravitational-wave detection candidate.

The unusually low χ^2 value put this event in a region of parameter space where the FAR extrapolation is not valid. This event happened to occur in a segment of time that we reserved in advance as a test data set, called a playground, that was not used in the rate limit calculation shown in the next section. See Sec. V for more details. We place a bound on its FAR of 1 per 4 years from the original 100 time-shift background estimate. We found that this candidate is not stable to small changes in our analysis pipeline. We were thus not able to measure its FAR independently using more time slides.

C. H2L1 event at GPS time 842749918.8057 (September 20, 2006 01:11:44.8057 GMT)

The third loudest event of this search at GPS time 842749918.8057 was found in H2 and L1. It was louder than any of the time-slide events in its two-month period. We put a bound on its FAR of 1.4/yr from our original analysis. An independent check using additional time slides yielded a FAR of 2.9/yr. We also interpolated and extrapolated the original 100 time-shift run to obtain a FAR of 1.9/yr.

The FAR of 1.9/yr was used in the upper limit calculation described in the next section. The L1 SNR and χ^2 is consistent with the background in that instrument. The H2 trigger is just above the SNR threshold of 5.5. This event is not rare. With a FAR of 1.9/yr, we expected to observe an event similar to this in our total observation time, even though it was above background in its local two-month H2L1 observation time. We conclude that this event is not a gravitational-wave detection candidate.

V. MERGER RATE LIMITS

Before examining events for detection candidates, we agreed upon the procedure described in this section for establishing an upper limit on the merger rate of black hole binaries if no detections were found.

In order to constrain the merger rate, we had to assess the sensitivity of the search. To test the detection sensitivity of our search pipeline, we injected $\sim 10^6$ signals into the detector strain data and processed it with the same pipeline used for the search. Events associated with the injected signals having FARs less than the loudest event of the search are considered to be found by the pipeline. We inject both EOB and phenomenological waveforms into the data. The injection parameters were as follows. For both waveform families, the injected signals had distances between 1 Mpc and 750 Mpc distributed uniformly in the logarithm of distance. Both families had a uniform distribution of sky location and orientation. For both families the total mass of the binary systems varied between 25–100 M_\odot . The component mass distributions, however, did differ between the EOB and phenomenological waveforms. The component mass distribution for EOB signals was generated by first producing a uniform distribution in the component masses between 1–99 M_\odot , and then clipping the distribution to have no systems outside of the total mass range 25–100 M_\odot . The mass distribution for the phenomenological waveforms was produced by first generating a distribution that was uniform in mass ratio ($m_1:m_2; m_1 \geq m_2$) between 1:1 and 10:1, and then clipping the result to have no systems outside of the total mass range 25–100 M_\odot .

As previously stated, we divided the ~ 2 years of data into 12 two-month periods and examined each of the three functioning detector combinations H1H2L1, H1L1, H2L1 separately for a total of 36 periods. We reserved 10% of the detector time as an unblinded *playground*: we do not use playground data in computing the upper limit on the merger rate. The second loudest event described in Sec. IV B happened to occur in the playground time. Using (3.8), we ranked each candidate event in the 36 periods. We used the loudest event in the foreground after category 3 vetoes in each period to establish a combined FAR threshold for determining what injections were found. For the events louder than background, we used the extrapolated FAR as agreed on prior to unblinding the analysis.

The efficiency $\bar{\epsilon}$ of recovering simulated signals in the detection pipeline is a function of the loudest event FAR, FAR^* , the radial distance to the source r and the masses m_1, m_2 . Note that in practice the mass dependence is captured by binning the mass plane into the boxes illustrated in Fig. 2. The bar denotes that the efficiency is averaged over sky position and orientation. We define the efficiency as

$$\bar{\epsilon}(\text{FAR}^*, r, m_1, m_2) = \frac{N_f(\text{FAR}^*, r, m_1, m_2)}{N_t(\text{FAR}^*, r, m_1, m_2)}, \quad (5.1)$$

where N_f is the number of found injections, N_t is the total number of injections and FAR^* is the FAR of the loudest event in a given analysis period. We then compute the volume of the sky surveyed in each of the 36 independent observation periods (denoted by the index i) by

$$V_i(m_1, m_2, \text{FAR}^*) = \int 4\pi r^2 \bar{\epsilon}_i(\text{FAR}^*, r, m_1, m_2) dr, \quad (5.2)$$

which has units of Mpc^3 . We estimate the variance

$$\sigma_i^2(m_1, m_2, \text{FAR}^*) = \langle V_i(m_1, m_2)^2 \rangle - \langle V_i(m_1, m_2) \rangle^2 \quad (5.3)$$

by bootstrapping the input injection distribution to account for Monte-Carlo errors as well as varying the injection distances according to the conservative quadrature sum

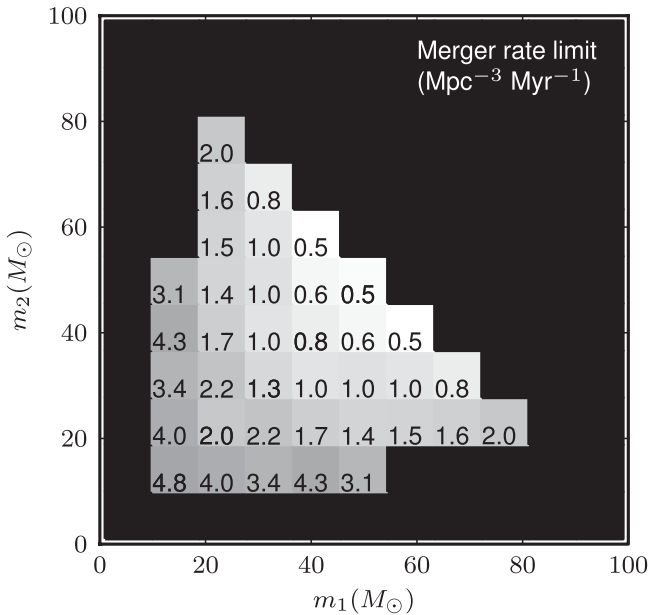


FIG. 2. The 90% confidence upper limit on the merger rate as a function of mass in units of M_\odot (symmetric over m_1 and m_2). This image represents the rate limit in units of $\text{Mpc}^{-3} \text{Myr}^{-1}$. These limits can be converted to traditional units of $L_{10}^{-1} \text{Myr}^{-1}$ by dividing by $0.0198 L_{10} \text{Mpc}^{-3}$ [99]. Only bins with mass ratios $<4:1$ have upper limits computed due to uncertainty in the waveform models for more asymmetric systems.

of the calibration uncertainty among the three detectors, 20% [133]. An additional systematic error is associated with uncertainty in the target waveforms. These limits are presented with our best understanding of the currently available waveforms. If we take the fractional difference in the SNRs of Phenomenological IMR and EOB waveforms, $\sim 10\%$ (see Sec. II C), as an indication of the uncertainty in the range due to imperfectly known waveforms, we conclude that the rates as reported in Fig. 2 have an additional systematic uncertainty of $\sim 30\%$. This uncertainty is not included in the rate estimates nor are any other systematic errors, for example, the accuracy of the waveform phasing. Some errors are discussed in [87,119].

In order to establish a merger rate $R(m_1, m_2)$ in units of mergers $\text{Mpc}^{-3} \text{yr}^{-1}$, we adopt formula (24) in [134]. It is important to note that some simplification of these formulas occurs when choosing the FAR as the ranking statistic [135]. Adapting the loudest event formalism described in [134] to our notation, if we constructed a posterior on R using only the results of a single analysis period, the marginalized likelihood function would be

$$p(k_i, \Omega_i, \Lambda_i | R) \propto \left[\frac{1}{(1 + R\Omega_i/k_i)^{k_i+1}} + \frac{R\Omega_i\Lambda_i(1 + 1/k_i)}{(1 + R\Omega_i/k_i)^{k_i+2}} \right] \quad (5.4)$$

where

$$\Omega_i = V_i(m_1, m_2, \text{FAR}^*) T_i, \quad (5.5)$$

$$k_i = \left[\frac{V_i(m_1, m_2, \text{FAR}^*)}{\sigma_i(m_1, m_2, \text{FAR}^*)} \right]^2, \quad (5.6)$$

$$\Lambda_i = \frac{d \ln[V_i(m_1, m_2, \text{FAR}^*)]}{d \text{FAR}^*} \frac{1}{T_i}, \quad (5.7)$$

T_i is the analyzed time for index i (assumed to have no errors), V_i is taken from (5.2), and the proportionality constant in (5.4) can depend on Ω_i, k_i and Λ_i , but not R .

In order to obtain the combined posterior probability distribution for the rate, given the sensitivities and loudest events of the 36 different analysis periods, labeled by the index i , we multiply the likelihood functions and assume an initial uniform prior on the rate. This results in a posterior probability of the form

$$p(R | m_1, m_2) \equiv p(R | \{k_i\}, \{\Omega_i\}, \{\Lambda_i\}) \propto p(\{k_i\}, \{\Omega_i\}, \{\Lambda_i\} | R) = \prod_i p(k_i, \Omega_i, \Lambda_i | R) \quad (5.8)$$

We integrate the normalized form of (5.8) to 90% to establish the 90% confidence upper limit on the merger rate (still a function of component mass), $R_{90\%}$. The result is given in Fig. 2. The upper limit in the lowest mass bin considered in this search is an order of magnitude higher than the most optimistic binary black hole merger rates

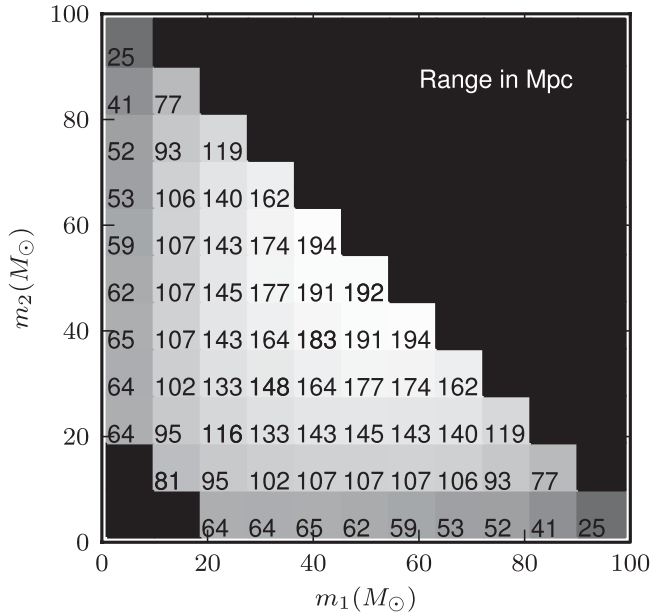


FIG. 3. Average range defined in (5.9) for the search in Mpc as a function of mass (symmetric over m_1 and m_2), assuming target waveforms that match the EOB and Phenomenological models.

predicted by current population-synthesis studies (see, e.g., [16,22,31]). At the upper end of the analyzed mass range, there are no reliable estimates for merger rates for intermediate-mass black holes, whose very existence remains to be confirmed; however, see [27–29,31] for some intriguing possibilities.

As discussed above, due to the uncertainties in the waveform models for asymmetric systems, we do not present upper limits for mass ratios $<4:1$. However, we do provide an average range for systems with smaller mass ratios based on the EOB and Phenomenological waveform models, in Fig. 3. The average range is defined as

$$\langle \mathcal{R}(m_1, m_2, \text{FAR}^*) \rangle = \frac{1}{\sum_i T_i} \sum_i T_i \mathcal{R}_i(m_1, m_2, \text{FAR}^*), \quad (5.9a)$$

$$\mathcal{R}_i(m_1, m_2, \text{FAR}^*) = \left[\frac{3}{4\pi} V_i(m_1, m_2, \text{FAR}^*) \right]^{1/3}, \quad (5.9b)$$

where $V_i(m_1, m_2, \text{FAR}^*)$ is defined in (5.2), \mathcal{R}_i is the radius of the sphere having volume of V_i and the average range $\langle \mathcal{R} \rangle$ is the time-weighted average of ranges computed from each of the ranges found by examining the loudest event in each of the 36 periods.

VI. CONCLUSIONS

We presented the result of a search for BBH coalescence during LIGO’s fifth science run spanning approximately two years of data taken from fall 2005 to fall 2007. We targeted binaries with total mass $M = m_1 + m_2$ in the range $25M_\odot \leq M \leq 100M_\odot$ and component masses of $1M_\odot \leq m_1, m_2 \leq 99M_\odot$ with negligible spin. In order to

effectually detect such systems with LIGO it was necessary to use template waveforms that encompass the inspiral, merger, and ringdown phases of compact binary coalescence. We employed two waveform families in this search to filter and assess the sensitivity. Both had been tuned to numerical relativity simulations.

We did not detect any plausible gravitational-wave candidates. However we estimated our search sensitivity and were able to constrain the merger rate of the targeted sources in the nearby universe. We established to 90% confidence that the merger rate of nonspinning black holes with component masses $19M_\odot \leq m_1, m_2 \leq 28M_\odot$ is less than $2.0 \text{ Mpc}^{-3} \text{ Myr}^{-1}$. We note that this is still about an order of magnitude higher than optimistic estimates for such systems [31] (see also [16,22]).

There are several limitations in the current approach. The main limitation is that the template waveforms neglect the effects of spin. Although the statistical distribution of the spins of black holes in binaries is not well known [136], there are examples of black holes in X-ray binaries which have been observed to have a large spin [137]. For a binary with spinning components, the expected observed gravitational-wave signal will differ from the nonspinning case; the observed duration can be different and there may be modulation of the gravitational-wave amplitude and phase. Neglecting such effects in the search templates will affect the detection efficiency for binaries with spinning components. We carried out a limited comparison between the ranges for nonspinning injections from which the upper limits are computed and spinning injections with aligned spins. The ranges agree to within $\sim 15\%$, i.e., within the confidence intervals on the ranges. This suggests that the loss of overlap with spinning waveforms is limited and may be partially compensated by the greater energy emitted by prograde spinning binaries. We have not yet investigated the effects of arbitrary spins, since no analytical inspiral-merger-ringdown waveforms for systems with generic spins were available at the time this search was conducted, but we hope to address the effects of spin more fully when evaluating the performance of future searches.

Another limitation of the search is that, due to the shorter duration and bandwidth of the signals in comparison to searches for lower mass systems, it is harder to distinguish between genuine signals and background events, since the signals themselves are more “glitchlike”. New approaches to the ranking of candidate events are being developed to improve the sensitivity of searches for these systems.

ACKNOWLEDGMENTS

The authors gratefully acknowledge the support of the United States National Science Foundation for the construction and operation of the LIGO Laboratory, the Science and Technology Facilities Council of the United Kingdom, the Max-Planck-Society, and the State of Niedersachsen/Germany for support of the construction

and operation of the GEO600 detector, and the Italian Istituto Nazionale di Fisica Nucleare and the French Centre National de la Recherche Scientifique for the construction and operation of the Virgo detector. The authors also gratefully acknowledge the support of the research by these agencies and by the Australian Research Council, the Council of Scientific and Industrial Research of India, the Istituto Nazionale di Fisica Nucleare of Italy, the Spanish Ministerio de Educación y Ciencia, the Conselleria d'Economia Hisenda i Innovació of the Govern de les

Illes Balears, the Foundation for Fundamental Research on Matter supported by the Netherlands Organisation for Scientific Research, the Polish Ministry of Science and Higher Education, the FOCUS Programme of Foundation for Polish Science, the Royal Society, the Scottish Funding Council, the Scottish Universities Physics Alliance, The National Aeronautics and Space Administration, the Carnegie Trust, the Leverhulme Trust, the David and Lucile Packard Foundation, the Research Corporation, and the Alfred P. Sloan Foundation.

-
- [1] B. Abbott *et al.* (LIGO Scientific Collaboration), *Rep. Prog. Phys.* **72**, 076901 (2009).
- [2] F. Acernese *et al.*, *Classical Quantum Gravity* **25**, 184001 (2008).
- [3] B. Abbott *et al.* (LIGO Scientific Collaboration), *Phys. Rev. D* **79**, 122001 (2009).
- [4] B. Abbott *et al.* (LIGO Scientific Collaboration), *Phys. Rev. D* **80**, 047101 (2009).
- [5] J. Abadie *et al.* (LIGO Scientific Collaboration and Virgo Collaboration), *Phys. Rev. D* **82**, 102001 (2010).
- [6] L. Blanchet, *Living Rev. Relativity* **5**, 3 (2002).
- [7] T. Futamase and Y. Itoh, *Living Rev. Relativity* **10**, 2 (2007).
- [8] The ISCO occurs at a gravitational-wave-frequency of $f_{\text{ISCO}} \approx 4.4 \times 10^3 \text{ Hz} \times (M/M_{\odot})^{-1}$ for a test particle orbiting a Schwarzschild black hole with mass M . Although the ISCO is only rigorously defined in the test-mass case, it serves as a convenient definition for the frequency of the onset of the merger epoch even for comparable masses.
- [9] R. A. Remillard and J. E. McClintock, *Annu. Rev. Astron. Astrophys.* **44**, 49 (2006).
- [10] J. A. Orosz, J. E. McClintock, R. Narayan, C. D. Bailyn, J. D. Hartman, L. Macri, J. Liu, W. Pietsch, R. A. Remillard, A. Shporer *et al.*, *Nature (London)* **449**, 872 (2007).
- [11] F. Ozel, D. Psaltis, R. Narayan, and J. E. McClintock, *Astrophys. J.* **725**, 1918 (2010).
- [12] W. M. Farr, N. Sravan, A. Cantrell, L. Kreidberg, C. D. Bailyn, I. Mandel, and V. Kalogera, *arXiv:1011.1459*.
- [13] T. Bulik and K. Belczyński, *Astrophys. J.* **589**, L37 (2003).
- [14] R. O’Shaughnessy, V. Kalogera, and K. Belczynski, *Astrophys. J.* **716**, 615 (2010).
- [15] P. A. Crowther, R. Barnard, S. Carpano, V. S. Dhillon, J. S. Clark, and A. M. T. Pollock, *Mon. Not. R. Astron. Soc.* **403**, L11 (2010).
- [16] T. Bulik, K. Belczynski, and A. Prestwich, *Astrophys. J.* **730**, 140 (2011).
- [17] R. M. O’Leary, R. O’Shaughnessy, and F. A. Rasio, *Phys. Rev. D* **76**, 061504 (2007).
- [18] A. Sadowski, K. Belczynski, T. Bulik, N. Ivanova, F. A. Rasio, and R. O’Shaughnessy, *Astrophys. J.* **676**, 1162 (2008).
- [19] M. C. Miller and V. M. Lauburg, *Astrophys. J.* **692**, 917 (2009).
- [20] R. M. O’Leary, B. Kocsis, and A. Loeb, *Mon. Not. R. Astron. Soc.* **395**, 2127 (2009).
- [21] K. Belczynski *et al.*, *Astrophys. J.* **714**, 1217 (2010).
- [22] K. Belczynski, M. Dominik, T. Bulik, R. O’Shaughnessy, C. Fryer, and D. E. Holz, *Astrophys. J.* **715**, L138 (2010).
- [23] M. C. Miller and E. J. M. Colbert, *Int. J. Mod. Phys. D* **13**, 1 (2004).
- [24] M. C. Miller, *Classical Quantum Gravity* **26**, 094031 (2009).
- [25] S. A. Farrell, N. A. Webb, D. Barret, O. Godet, and J. M. Rodrigues, *Nature (London)* **460**, 73 (2009).
- [26] D. A. Brown, J. Brink, H. Fang, J. R. Gair, C. Li, G. Lovelace, I. Mandel, and K. S. Thorne, *Phys. Rev. Lett.* **99**, 201102 (2007).
- [27] I. Mandel, D. A. Brown, J. R. Gair, and M. C. Miller, *Astrophys. J.* **681**, 1431 (2008).
- [28] J. M. Fregeau, S. L. Larson, M. C. Miller, R. O’Shaughnessy, and F. A. Rasio, *Astrophys. J.* **646**, L135 (2006).
- [29] P. Amaro-Seoane and M. Freitag, *Astrophys. J.* **653**, L53 (2006).
- [30] K. Belczynski, T. Bulik, and B. Rudak, *Astrophys. J.* **608**, L45 (2004).
- [31] J. Abadie *et al.* (LIGO Scientific Collaboration and Virgo Collaboration), *Classical Quantum Gravity* **27**, 173001 (2010).
- [32] S. G. Hahn and R. W. Lindquist, *Ann. Phys. (N.Y.)* **29**, 304 (1964).
- [33] F. Pretorius, *Phys. Rev. Lett.* **95**, 121101 (2005).
- [34] M. Campanelli, C. O. Lousto, P. Marronetti, and Y. Zlochower, *Phys. Rev. Lett.* **96**, 111101 (2006).
- [35] J. G. Baker, J. Centrella, D.-I. Choi, M. Koppitz, and J. van Meter, *Phys. Rev. Lett.* **96**, 111102 (2006).
- [36] F. Pretorius, in *Physics of Relativistic Objects in Compact Binaries: from Birth to Coalescence*, edited by M. Colpi, P. Casella, V. Gorini, U. Moschella, and A. Possenti (Springer, Heidelberg, Germany, 2009).
- [37] S. Husa, *Eur. Phys. J. Special Topics* **152**, 183 (2007).
- [38] M. Hannam, *Classical Quantum Gravity* **26**, 114001 (2009).
- [39] I. Hinder, *Classical Quantum Gravity* **27**, 114004 (2010).

- [40] J.M. Centrella, J.G. Baker, B.J. Kelly, and J.R. van Meter, *Rev. Mod. Phys.* **82**, 3069 (2010).
- [41] B. Aylott *et al.*, *Classical Quantum Gravity* **26**, 165008 (2009).
- [42] F. Herrmann, I. Hinder, D. Shoemaker, and P. Laguna, *Classical Quantum Gravity* **24**, S33 (2007).
- [43] J.G. Baker *et al.*, *Astrophys. J.* **653**, L93 (2006).
- [44] J.A. Gonzalez, U. Sperhake, B. Brügmann, M. Hannam, and S. Husa, *Phys. Rev. Lett.* **98**, 091101 (2007).
- [45] F. Herrmann, I. Hinder, D. Shoemaker, P. Laguna, and R.A. Matzner, *Astrophys. J.* **661**, 430 (2007).
- [46] M. Koppitz *et al.*, *Phys. Rev. Lett.* **99**, 041102 (2007).
- [47] M. Campanelli, C.O. Lousto, Y. Zlochower, and D. Merritt, *Astrophys. J.* **659**, L5 (2007).
- [48] J.A. Gonzalez, M.D. Hannam, U. Sperhake, B. Brügmann, and S. Husa, *Phys. Rev. Lett.* **98**, 231101 (2007).
- [49] W. Tichy and P. Marronetti, *Phys. Rev. D* **76**, 061502 (2007).
- [50] M. Campanelli, C.O. Lousto, Y. Zlochower, and D. Merritt, *Phys. Rev. Lett.* **98**, 231102 (2007).
- [51] J.G. Baker *et al.*, *Astrophys. J.* **668**, 1140 (2007).
- [52] F. Herrmann, I. Hinder, D.M. Shoemaker, P. Laguna, and R.A. Matzner, *Phys. Rev. D* **76**, 084032 (2007).
- [53] B. Brügmann, J.A. Gonzalez, M. Hannam, S. Husa, and U. Sperhake, *Phys. Rev. D* **77**, 124047 (2008).
- [54] J.D. Schnittman *et al.*, *Phys. Rev. D* **77**, 044031 (2008).
- [55] D. Pollney *et al.*, *Phys. Rev. D* **76**, 124002 (2007).
- [56] C.O. Lousto and Y. Zlochower, *Phys. Rev. D* **77**, 044028 (2008).
- [57] J.G. Baker *et al.*, *Astrophys. J.* **682**, L29 (2008).
- [58] S. Dain, C.O. Lousto, and Y. Zlochower, *Phys. Rev. D* **78**, 024039 (2008).
- [59] J. Healy, F. Herrmann, I. Hinder, D.M. Shoemaker, P. Laguna, and R.A. Matzner, *Phys. Rev. Lett.* **102**, 041101 (2009).
- [60] J.A. Gonzalez, U. Sperhake, and B. Brügmann, *Phys. Rev. D* **79**, 124006 (2009).
- [61] M. Campanelli, C.O. Lousto, and Y. Zlochower, *Phys. Rev. D* **74**, 084023 (2006).
- [62] M. Campanelli, C.O. Lousto, Y. Zlochower, B. Krishnan, and D. Merritt, *Phys. Rev. D* **75**, 064030 (2007).
- [63] E. Berti *et al.*, *Phys. Rev. D* **76**, 064034 (2007).
- [64] L. Rezzolla *et al.*, *Astrophys. J.* **679**, 1422 (2008).
- [65] L. Boyle, M. Kesden, and S. Nissanke, *Phys. Rev. Lett.* **100**, 151101 (2008).
- [66] L. Rezzolla *et al.*, *Astrophys. J.* **674**, L29 (2008).
- [67] P. Marronetti, W. Tichy, B. Brügmann, J. Gonzalez, and U. Sperhake, *Phys. Rev. D* **77**, 064010 (2008).
- [68] U. Sperhake *et al.*, *Phys. Rev. D* **78**, 064069 (2008).
- [69] I. Hinder, B. Vaishnav, F. Herrmann, D. Shoemaker, and P. Laguna, *Phys. Rev. D* **77**, 081502 (2008).
- [70] E. Berti, V. Cardoso, J.A. Gonzalez, U. Sperhake, and B. Brügmann, *Classical Quantum Gravity* **25**, 114035 (2008).
- [71] L. Boyle and M. Kesden, *Phys. Rev. D* **78**, 024017 (2008).
- [72] W. Tichy and P. Marronetti, *Phys. Rev. D* **78**, 081501 (2008).
- [73] L. Rezzolla, *Class. Quant. Grav.* **26**, 094023 (2009); *Proceedings of 7th LISA Symposium, Barcelona 2008*, edited by L. Rezzolla. [*Classical Quantum Gravity* **22**, 10 (2005)].
- [74] A. Buonanno, L.E. Kidder, and L. Lehner, *Phys. Rev. D* **77**, 026004 (2008).
- [75] M. Hannam, S. Husa, J.G. Baker, M. Boyle, B. Brügmann, T. Chu, N. Dorband, F. Herrmann, I. Hinder, B.J. Kelly *et al.*, *Phys. Rev. D* **79**, 084025 (2009).
- [76] J.G. Baker, J.R. van Meter, S.T. McWilliams, J. Centrella, and B.J. Kelly, *Phys. Rev. Lett.* **99**, 181101 (2007).
- [77] M. Hannam *et al.*, *Phys. Rev. D* **77**, 044020 (2008).
- [78] M. Boyle *et al.*, *Phys. Rev. D* **76**, 124038 (2007).
- [79] M. Hannam, S. Husa, B. Brügmann, and A. Gopakumar, *Phys. Rev. D* **78**, 104007 (2008).
- [80] M. Campanelli, C.O. Lousto, H. Nakano, and Y. Zlochower, *Phys. Rev. D* **79**, 084010 (2009).
- [81] M. Boyle *et al.*, *Phys. Rev. D* **78**, 104020 (2008).
- [82] I. Hinder, F. Herrmann, P. Laguna, and D. Shoemaker, *Phys. Rev. D* **82**, 024033 (2010).
- [83] T. Chu, H.P. Pfeiffer, and M.A. Scheel, *Phys. Rev. D* **80**, 124051 (2009).
- [84] D. Pollney, C. Reisswig, E. Schnetter, N. Dorband, and P. Diener, *Phys. Rev. D* **83**, 044045 (2011).
- [85] A. Buonanno, G.B. Cook, and F. Pretorius, *Phys. Rev. D* **75**, 124018 (2007).
- [86] Y. Pan, A. Buonanno, J.G. Baker, J. Centrella, B.J. Kelly, S.T. McWilliams, F. Pretorius, and J.R. van Meter, *Phys. Rev. D* **77**, 024014 (2008).
- [87] A. Buonanno *et al.*, *Phys. Rev. D* **76**, 104049 (2007).
- [88] T. Damour, A. Nagar, E.N. Dorband, D. Pollney, and L. Rezzolla, *Phys. Rev. D* **77**, 084017 (2008).
- [89] T. Damour, A. Nagar, M. Hannam, S. Husa, and B. Brügmann, *Phys. Rev. D* **78**, 044039 (2008).
- [90] M. Boyle, A. Buonanno, L.E. Kidder, A.H. Mroué, Y. Pan, H.P. Pfeiffer, and M.A. Scheel, *Phys. Rev. D* **78**, 104020 (2008).
- [91] T. Damour and A. Nagar, *Phys. Rev. D* **79**, 081503 (2009).
- [92] A. Buonanno, Y. Pan, H.P. Pfeiffer, M.A. Scheel, L.T. Buchman, and L.E. Kidder, *Phys. Rev. D* **79**, 124028 (2009).
- [93] P. Ajith *et al.*, *Classical Quantum Gravity* **24**, S689 (2007).
- [94] P. Ajith, M. Hannam, S. Husa, Y. Chen, B. Bruegmann, N. Dorband, D. Mueller, F. Ohme, D. Pollney, C. Reisswig *et al.*, [arXiv:0909.2867](https://arxiv.org/abs/0909.2867).
- [95] L. Santamaria, F. Ohme, P. Ajith, B. Bruegmann, N. Dorband, M. Hannam, S. Husa, P. Moesta, D. Pollney, C. Reisswig *et al.*, *Phys. Rev. D* **82**, 064016 (2010).
- [96] L. Cadonati *et al.*, *Classical Quantum Gravity* **26**, 114008 (2009), <http://stacks.iop.org/0264-9381/26/i=11/a=114008>.
- [97] B. Abbott *et al.* (LIGO Scientific Collaboration), *Phys. Rev. D* **73**, 062001 (2006).
- [98] B. Abbott *et al.* (LIGO Scientific Collaboration), *Phys. Rev. D* **77**, 062002 (2008).
- [99] R.K. Kopparapu, C. Hanna, V. Kalogera, R. O'Shaughnessy, G. Gonzalez, P.R. Brady, and S. Fairhurst, *Astrophys. J.* **675**, 1459 (2008).
- [100] A. Buonanno, Y. Chen, and M. Vallisneri, *Phys. Rev. D* **67**, 024016 (2003); **74**, 029903(E) (2006).
- [101] B. Abbott *et al.* (LIGO Scientific Collaboration), *Phys. Rev. D* **78**, 042002 (2008).
- [102] B. Abbott *et al.* (LIGO Scientific Collaboration), *Phys. Rev. D* **80**, 062001 (2009).

- [103] C. Cutler *et al.*, *Phys. Rev. Lett.* **70**, 2984 (1993).
- [104] H. Tagoshi and M. Sasaki, *Prog. Theor. Phys.* **92**, 745 (1994).
- [105] L. Blanchet, T. Damour, B. R. Iyer, C. M. Will, and A. G. Wiseman, *Phys. Rev. Lett.* **74**, 3515 (1995).
- [106] L. Blanchet, G. Faye, B. R. Iyer, and B. Joguelet, *Phys. Rev. D* **65**, 061501 (2002).
- [107] L. Blanchet, T. Damour, G. Esposito-Farèse, and B. R. Iyer, *Phys. Rev. Lett.* **93**, 091101 (2004).
- [108] D. J. A. McKechnan, C. Robinson, and B. S. Sathyaprakash, *Classical Quantum Gravity* **27**, 084020 (2010).
- [109] A. Buonanno and T. Damour, *Phys. Rev. D* **59**, 084006 (1999).
- [110] A. Buonanno and T. Damour, *Phys. Rev. D* **62**, 064015 (2000).
- [111] T. Damour, P. Jaranowski, and G. Schäfer, *Phys. Rev. D* **62**, 084011 (2000).
- [112] T. Damour, B. R. Iyer, P. Jaranowski, and B. S. Sathyaprakash, *Phys. Rev. D* **67**, 064028 (2003).
- [113] T. Damour, B. R. Iyer, and B. S. Sathyaprakash, *Phys. Rev. D* **57**, 885 (1998).
- [114] T. Damour, B. R. Iyer, and A. Nagar, *Phys. Rev. D* **79**, 064004 (2009).
- [115] Y. Pan, A. Buonanno, M. Boyle, L. Buchman, L. Kidder, H. P. Pfeiffer, and M. Scheel (2011) (to be published).
- [116] We note that Ref. [87] contains a typo and should read $D_4^0(r) = \frac{r^4}{r^3 + 6\eta r^2 + 2\eta(26 - 3\eta)r + 36\eta^2}$
- [117] T. Damour and A. Gopakumar, *Phys. Rev. D* **73**, 124006 (2006).
- [118] E. Berti, V. Cardoso, and C. M. Will, *Phys. Rev. D* **73**, 064030 (2006).
- [119] P. Ajith *et al.*, *Phys. Rev. D* **77**, 104017 (2008).
- [120] B. Bruegmann, J. A. Gonzalez, M. Hannam, S. Husa, U. Sperhake, and W. Tichy, *Phys. Rev. D* **77**, 024027 (2008).
- [121] P. Ajith, *Classical Quantum Gravity* **25**, 114033 (2008).
- [122] B. Allen, *Phys. Rev. D* **71**, 062001 (2005).
- [123] T. Cokelaer, *Phys. Rev. D* **76**, 102004 (2007).
- [124] B. J. Owen, *Phys. Rev. D* **53**, 6749 (1996).
- [125] S. Babak, Balasubramanian, D. Churches, T. Cokelaer, and B. Sathyaprakash, *Classical Quantum Gravity* **23**, 5477 (2006).
- [126] B S Sathyaprakash and V S Dhurandhar, *Phys. Rev. D* **44**, 3819 (1991).
- [127] Strictly speaking, the chirp times τ_0 and τ_3 [123].
- [128] C. A. K. Robinson, B. S. Sathyaprakash, and A. S. Sengupta, *Phys. Rev. D* **78**, 062002 (2008).
- [129] J. Slutsky *et al.*, *Classical Quantum Gravity* **27**, 165023 (2010).
- [130] In fact the analysis of the last six months of data in this search used an additional discriminator called the r^2 veto, which checks the consistency of the χ^2 time series [131]
- [131] A. Rodríguez, Master's thesis, Louisiana State University, 2007.
- [132] Since H1 and H2 are colocated and have the same antenna patterns, this ratio can be estimated independent of geometrical effects.
- [133] J. Abadie *et al.* (LIGO Scientific Collaboration), *Nucl. Instrum. Methods Phys. Res., Sect. A* **624**, 223 (2010).
- [134] R. Biswas, P. R. Brady, J. D. E. Creighton, and S. Fairhurst, *Classical Quantum Gravity* **26**, 175009 (2009).
- [135] D. Keppel, Ph.D. thesis, Caltech, Pasadena, CA 2009, <http://resolver.caltech.edu/CaltechETD:etd-05202009-115750>.
- [136] I. Mandel and R. O'Shaughnessy, *Classical Quantum Gravity* **27**, 114007 (2010).
- [137] J. E. McClintock *et al.*, *Astrophys. J.* **652**, 518 (2006).